Intermediate states of graphene nanoribbons

Benjamin Alldritt

School of Science

Thesis submitted for examination for the degree of Master of Science in Technology.

Otaniemi 22.05.2017

Thesis supervisor:

Prof. Peter Liljeroth

Thesis advisor:

D.Sc. (Tech.) Fabian Schultz

Aalto University
School of Science

AALTO UNIVERSITY
SCHOOL OF SCIENCE

ABSTRACT OF THE
MASTER'S THESIS

Author: Benjamin Alldritt

Title: Intermediate states of graphene nanoribbons

Date: 22.05.2017 Language: English Number of pages: 5+44

Depart of Applied Physics

Professorship: Atomic Scale Physics

Supervisor: Prof. Peter Liljeroth

Advisor: D.Sc. (Tech.) Fabian Schultz

The down-scaling of Si CMOS devices has encountered challenges related power and heat dissipation resulting in the need for new material selection. The use of single molecules, such as graphene nanoribbons (GNR), as transistors or device interconnects holds the possibility of significantly improving the performance and power consumption of consumer electronic devices. Recent developments in the synthesis of graphene nanoribbons have allowed for atomically precise construction via on-surface synthesis from molecular precursors. While the precursor toolbox for different GNRs has expanded rapidly, specific reaction pathways and the role of the catalytic metal substrate in the GNR growth have not yet been worked out in detail.

In this work, low-temperature evaporation of planar dibromoperylene (DBP) was performed on a Cu(111) surface to determine the reaction pathway from individual DBP monomers to GNR formation. With controlled annealing, it was possible to synthesize intermediate structures step by step. Scanning tunneling microscopy (STM), non-contact atomic force microscopy (nc-AFM), and Kelvin-probe force microscopy (KPFM) experiments performed at low-temperature were used to confirm the evolution of the intermediate states to armchair nanoribbons. We find that the interaction between the Cu(111) surface and the DBP precursor influences the resulting GNR structure. The intermediate structures formed are stabilized by the Cu(111) substrate and further annealing results in armchair GNR formation.

Keywords: Graphene, Self-Assembly, Scanning Tunneling Microscopy, Atomic Force Microscopy, Kelvin Probe Force Microscopy, Ullmann Coupling

Acknowledgments

None of us journey through life alone and there are many that I want to thank for their time and dedication for assisting me to this point. First, I thank Prof. Peter Liljeroth and my instructor Dr. Fabian Schultz for their guidance and patience during the writing of my Master's thesis. Both have been excellent mentors, providing advice, guidance, papers, criticism and experiences in experimental physics. Additionally, I would like to thank the many members of the Atomic Scale Physics group, particularly Avijit Kumar and Shawulienu Kezilebieke, for their assistance and helping fix the many issues encountered.

I also extend thanks to my family for all of their support since I embarked on this journey in Finland. Thank you to the Fulbright program for allowing me to come to Finland many years ago to begin a new career as well as to all of those friends, including Dustin, Daniel, and Win, who encouraged me to pursue this path. Finally, a most sincere thank you to my partner, Maarit Sallanko, for all of her support these past few years and keeping the light on during all those late nights.

Otaniemi, 22.05.2017

Benjamin W. Alldritt

Contents

Abbreviations

AFM	Atomic Force Microscope
CPD	Contact Potential Difference
CVD	Chemical Vapor Deposition
DBP	Dibromoperylene
DOS	Density of States
FCC	Face Centered Cubic
FET	Field Effect Transistor
GNR	Graphene Nanoribbon
KPFM	Kelvin Probe Force Microscopy
LCPD	Local Contact Potential Difference
LDOS	Local Density of States
LEED	Low Energy Electron Diffraction
MOSFET	Metal-Oxide-Semiconductor Field Effect Transistor
QMS	Quadropol Mass Spectrometer
RT	Room Temperature
SEM	Scanning Electron Microscopy
Si CMOS	Silicon Complementary Metal-Oxide-Semiconductor
STM	Scanning Tunneling Microscope
STS	Scanning Tunneling Spectroscopy
TEM	Transmission Electron Microscopy
UHV	Ultra-High Vacuum

1 Introduction

At present, we have begun to see the limits of Moore's Law [1], which states that the number of transistors on a computer chip will double every two years. The 10 nm chip class represents the most current level of manufacturing available from Samsung and Intel [2], some of the world's largest semiconductor chip manufacturers. Further scaling-down of silicon complementary metal-oxide-semiconductor (Si CMOS) is challenged by power dissipation or more specifically, short-channel effects such as gate leakage current or an impaired drain-current saturation [3]. Minimum transistor size is impacted by these limitations and will continue to affect future chip designs. The need for alternative methods led to the development of molecular electronics. The use of a single molecule as a rectifier was proposed initially by Aviram and Ratner in 1974 [4], then realized in 1990 and 1993 by Sambles and Ashwell, later confirmed by Metzger in 1997 [5, 6, 7]. Molecular electronics now can be seen as a potential way of extending Moore's law beyond the current limitations, allowing for the replacement of not just individual components, but also the interconnects between them.

Graphene nanoribbons (GNR) hold the possibility to significantly improve the performance of nanoscale electronic devices due to the high carrier mobility in graphene, a single layer of carbon atoms arranged in a honeycomb lattice structure [8]. Ribbon width modification allows for control over the bandgap, where the bandgap scales inversely with the width of the ribbon [9]. The band gap is a result of quantum confinement in GNRs, as infinite graphene does not possess a band gap. Realization of graphene nanoribbons with desired properties requires a control of the structures, long-range order, and other features. In addition to ribbon width, the symmetry and atomic structure of the edge influences the electronic properties of GNRs. In Fig 1.1 (a), two edge types are seen: armchair and zigzag, each with a particular local electronic state [10].

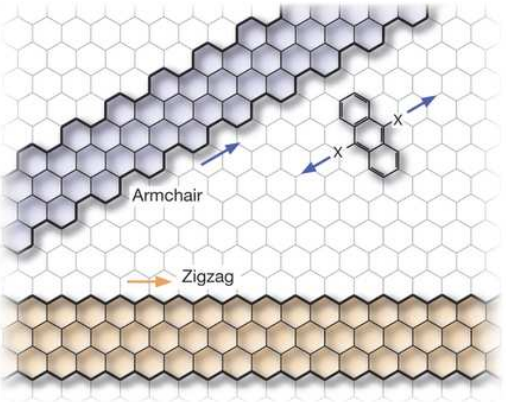

(a)

Figure 1.1: (a) Armchair and zigzag graphene nanoribbons structures. Reprinted with permission from [11]

In order to prepare GNRs, two approaches are available: top-down and bottom-up.

On a large scale, top-down methods for production of atomically precise graphene nanoribbons, such as lithography and etching, are challenging to achieve. Additionally, with the top-down approach results in chemical modifications to the edge structure, potentially creating undesirable edge states. Finally, even with precise methods in the lithographic and etching techniques, they result in an edge roughness of 5nm, limiting the properties of the produced graphene nanoribbons [12].

Alternatively, bottom-up fabrication [13] [14], where atomically precise nanostructures are constructed from molecular precursors through on-surface chemical reactions or self-assembly, presents a method where precise design is possible. An example of bottom-up fabrication is seen in Fig 1.2, where In this thesis, we study the different intermediates states occurring during for the formation of GNRs through an on-surface Ullmann coupling reaction.

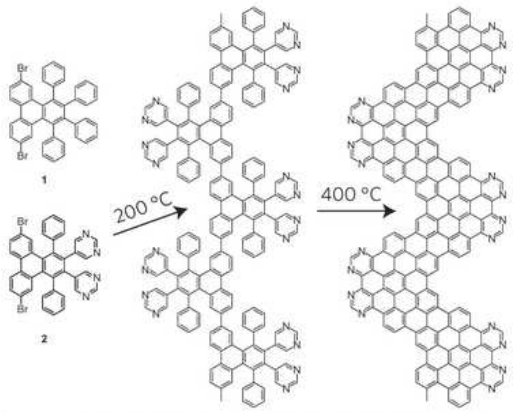

(a)

Figure 1.2: (a) An example of bottom-up fabrication of graphene heterojunctions from individual unit monomer to chevron nanoribbons. Reprinted with permission from [15]

The energy barriers for the different reaction steps will depend on the metal surface which is used to carry out the synthesis, because the interaction with the surface determines the catalytic activity and adsorption geometry. This is most evident from results for dibromo-bianthryl precusors, which result in armchair ribbons on Au(111) and Ag(111), but yield chiral ribbons on Cu(111) [16] [17] [18]. This difference between the metal surfaces and the molecules themselves all play a role in the reaction pathway, where careful design of the molecule and the surface can yield new understanding into nanostructure formation.

Usage of the bottom-up method has been enhanced significantly with the development of scanning tunneling microscopy (STM). Controllable environmental conditions in ultra-high vacuum avoids on-surface chemical reactions from other solvents, gases or contaminants. Additionally, with STM, it is possible to observe the transformations of the monomers during the intermediate states prior to the formation of GNRs. Combined with atomic force microscopy (AFM) and Kelvin probe force microscopy (KPFM), it is possible to identify the individual atoms and

map the electronic state of the local structures. By depositing monomers on the surface and varying the temperature, it is possible to see the intermediate states that exist prior to formation of the GNR.

The goal of this thesis is to probe the intermediate states of formation of graphene nanoribbons with planar 3,9(10) dibromoperylene (DBP) and characterize the types of structures that can be formed. DBP is known to yield the same armchair GNRs on both Au(111) and Cu(111)[19][18]. However, in contrast to Au(111)[F. Schulz and P. Liljeroth, in preparation], on Cu(111) the various intermediates are formed at distinctively different temperatures and yet the resulting ribbons are of low quality [18]. In order to gain more insight into the structures of these intermediates and shine light on how they influence the entire reaction path, 5-atom wide armchair GNRs will be prepared on Cu(111) substrate with precursor molecules deposited on the surface and annealed at different temperatures. In the Background section, an overview of the theory and operational principles of various scanning probe microscopy methods will be made. In the Experimental Setup, an overview of the equipment settings and details will be reviewed. Results and Discussion documents all of the data collected from the experiments and discusses the major findings from the experiments. The thesis concludes with the Conclusion and Future Work section by providing further context on the meaning of the results and how they can be applied.

2 Background

This chapter provides an overview of the basics of scanning tunneling microscopy. Section 2.1 addresses the principles of operation, theoretical foundations for STM, quantum mechanical tunneling, and other background information that will be critical to understand the operation of an STM. Section 2.2 reviews over the theoretical background of atomic force microscopy, the forces involved, operating modes, and tip modification. Section 2.3 addresses the Kelvin probe force microscopy, its connections to AFM, and the theoretical framework.

2.1 Introduction to Scanning Tunneling Microscopy

The imaging of individual atoms was a challenge prior to the invention of the STM. Spectroscopy, using information gathered from reciprocal space, was the dominate method for surface science. However, these methods were limited to approximately 100 Å resolution due to the finite coherence of the beam and relied primarily on scattering or diffraction [20]. This led to the development of a real space imaging technique called scanning electron microscopy (SEM) which, using a tightly focused electron beam, scans over a surface to generate an image. While achieving resolutions less than 2 Å [20], SEM was limited by its need for conductive structures and vacuum requirements.

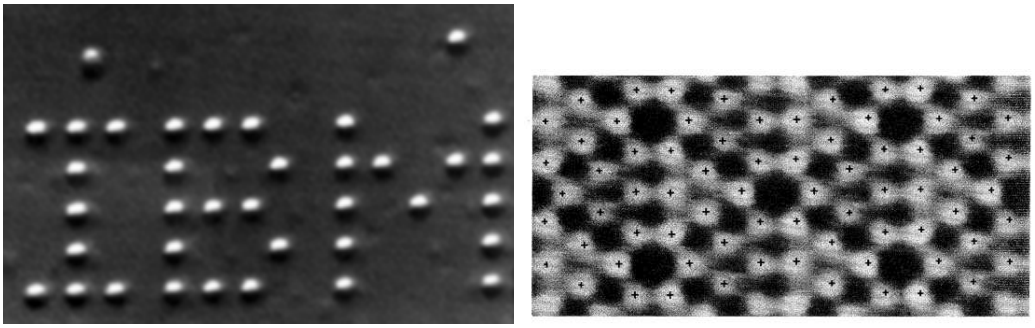

(a) (b)

Figure 2.1: (a) Manipulation of 35 Xe atoms to spell IBM. Reprinted with permission from [21]. (b) First real-space Si(111)(7x7) reconstruction with STM. Reprinted with permission from [22].

STM was invented by Binning and Rohrer in 1982 [23] as a real space imaging technique and in 1986 they were awarded the Nobel Prize in Physics for their design of the scanning tunneling microscope. This technique allowed for sub-nanometer resolution when imaging surfaces of conducting and semi-conducting, such as Si, samples in real space and simultaneously allowed for researchers to manipulate atoms and molecules (Fig 2.2 (a)) [21]. In 1983, the structure of Si(111)(7x7) surface reconstruction (Fig 2.2 (b)) was observed and explained, marking a major achievement for STM [22]. Additionally, STM allows for the study of local electronic properties down to the atomic scale, such as the local density of states (LDOS). In

1985, scanning tunneling spectroscopy (STS) was used to observe the surface state of Si(111)(7x7), where the dI/dV information obtained was proportional to the LDOS [24]. One of the major factors in obtaining high quality images using STM is the tip quality, more specifically structure of the tip apex. The theory underlying STM is quantum mechanical tunneling, which describes the tunneling of particles through a classically-forbidden potential barrier. The tip apex can be influenced by the location of other atoms, causing a change in the signal. For instance, if a CO molecule is attached to the tip apex, tunneling will occur through the degenerated π_x and π_y orbitals [25]. The result is an increase in the p-wave contributions for the tunneling current and an improvement in resolution. Due to its ability to not only identify and image structures on a surface, but also manipulate those structures, STM is a useful technique to research nanostructures with atomic resolution.

2.1.1 Principles of Operation

The STM setup consists of a sample and an atomically sharp probe tip attached to a series of piezo elements. The piezoelectric effect refers to the application of voltage on certain materials that cause material deformation, allowing for high accuracy tip positioning. Tip positioning is adjusted laterally (x,y directions) and vertically (z direction) by these piezos. The topography of the sample surface is determined by the change in magnitude of the current between the tip and the sample where a bias voltage is applied between them. The STM images the surface by scanning the tip across the sample, where, at every point, the current and tip-sample distance are recorded. In order to achieve atomic resolution of a surface, such as Cu(111), the scanning tip must be sensitive enough and controllable with high precision.

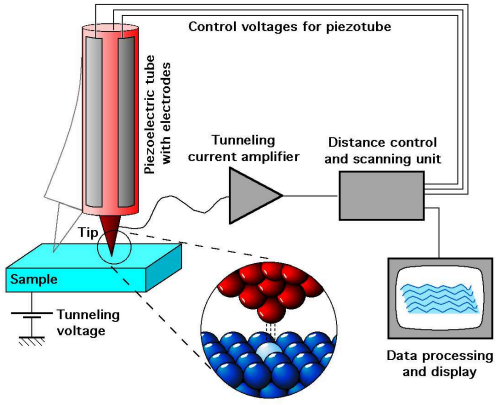

(a)

Figure 2.2: (a) Schematic diagram of a scanning tunneling microscope Reprinted with permission from Michael Schmid, TU-Wien.

The tip and the sample are separated by a few Ångstrom, resulting in an overlap of the electron wavefunctions of the tip and sample, allowing the electrons to tunnel through the vacuum barrier. Tunneling requires that the electrons cross the potential barrier introduced by the vacuum gap. Looking at a simplified one-dimensional

model, should the electron energy be lower than that of the potential barrier, the probability of electron crossing it will decay exponentially with the potential width. If a bias voltage, V_{bias}, is applied, the tunneling current depends upon the electronic states between Fermi energy and the contribution of V_{bias}. The following relation in Eq. 2.1 describes the exponential dependence of the tunneling current I on the tip-sample distance z:

$$I \propto I_0 e^{-2\kappa z} \tag{2.1}$$

$$\kappa = \frac{\sqrt{2m(U - V_e)}}{\hbar} \tag{2.2}$$

m is the electron mass, U is the barrier potential, V_e is the electron energy, and $\hbar$ is reduced Planck's constant. The relation is sensitive to minor changes in the tip-sample distance, which has a large impact on the tunneling current. To demonstrate this, if the current work function is represented as a value of approximately 5eV, the current changes by one order of magnitude if the tip-sample distance is change by 1 Å. In Fig 2.3, the potential barrier model is shown as well as the tunneling through vacuum barrier between the tip and the sample. At low bias values, the work function, then $U - V_e$ will approximately equal the work function of the sample. Additionally, the small bias values will result in the electron states with an eV of the Fermi energy are excited, so tunneling will occur by the electrons near the Fermi energy. This is one of the reasons why STM is able to achieve atomic level resolution.

STM operation occurs through two common operation modes, constant height mode and constant current mode. In constant height mode, the sample surface is scanned by the tip at a fixed distance between the tip and the sample surface while the tunneling current is recorded. In constant current mode, a fixed set point for the tunneling current is kept by varying the height of the tip as it is scanned over the sample surface. One of the challenges in interpretation of the signal is that the topographic images are not necessarily the same as the actual surface curvature, particularly in the case of constant-current scans. Instead, it is the convolution of the tip and the local electronic states of the sample [27].

2.1.2 Quantum Mechanical Tunneling and Square Potential

In the classical picture for a one-dimensional (1D) potential barrier, an electron in a potential well V(z) is described as

$$\frac{p^2}{2m} + V(z) = E \tag{2.3}$$

where p is the electron momentum, m is the electron mass and E is the energy. Particles can only cross the barrier when E > V(z), meaning that for E < V(z), it represents an impenetrable barrier. In the quantum mechanical picture where a particle can be described by a wave function, a particle with an energy lower than that of the barrier has a probability of tunneling through the barrier. This probability is dependent on the barrier width.

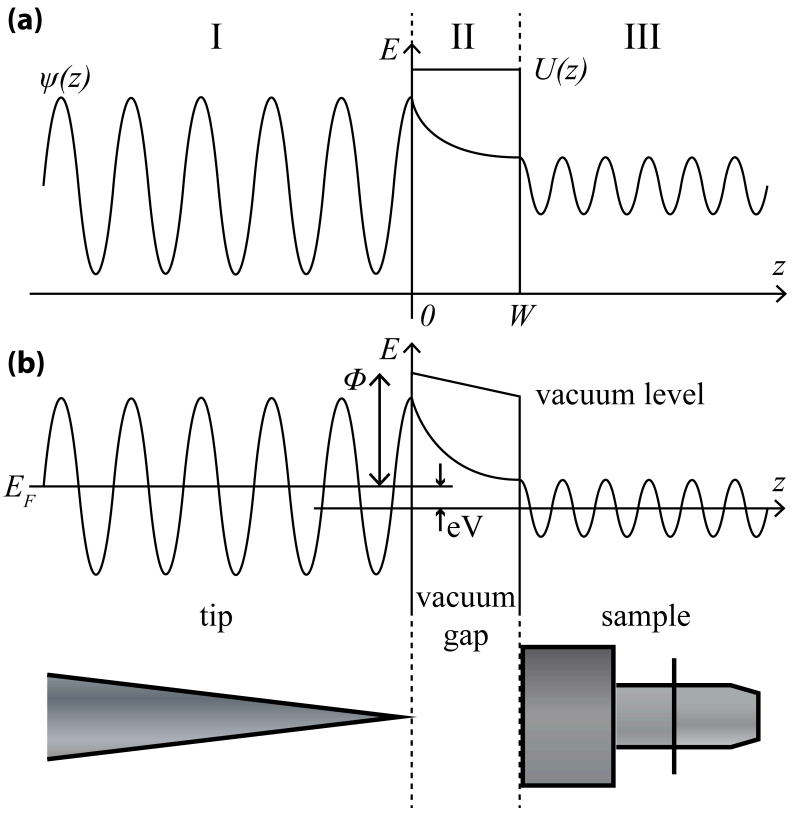

(a)

Figure 2.3: (a) Diagram of a one-dimensional potential barrier. (b) Diagram of the tunneling from a tip to the sample through the vacuum barrier in an STM. Reprinted with permission from [26]

Solving this problem requires separating the problem into three components, the two sides of the potential barrier and the barrier itself. The left barrier defined by the following wavefunction:

$$\Psi_L = e^{ikz} + Le^{-ikz}, k = \sqrt{\frac{2mE}{\hbar^2}} \tag{2.4}$$

which represents the incoming wave and the reflected wave. In order to calculate the probability of the electron to tunnel across the barrier, the following Schrödinger equation needs to be solved:

$$-\frac{\hbar^2}{2m}\frac{d^2}{dz^2}\Psi(z) + V(z)\Psi(z) = E\Psi(z) \tag{2.5}$$

where h is the reduced Planck constant, m is the electron mass, and z is the position. In contrast to the classical picture of Eq. (2.3), the momentum is now given as an operator $-i\hbar d/dz$ acting on the electron's wavefunction $\Psi(z)$. For a free particle and

assuming the potential outside the barrier is zero, it is represented by the following equation:

$$-\frac{\hbar^2}{2m}\frac{d^2}{dz^2}\Psi_L = E\Psi_L \tag{2.6}$$

In the barrier region, the wavefunction is represented by

$$\Psi_B = Ae^{i\omega z} + Be^{-i\omega z}, \omega = \sqrt{\frac{2m(V_0 - E)}{\hbar^2}} \tag{2.7}$$

yielding for a rectangular shaped barrier of height U_0

$$-\frac{\hbar^2}{2m}\frac{d^2}{dz^2}\Psi_B + V_0\Psi_B = E\Psi_B \tag{2.8}$$

For the right side of the barrier, the wave function leaving the barrier is defined as:

$$\Psi_{RT} = Te^{iqz}, q = \sqrt{\frac{2m(V_0 - E)}{\hbar^2}} \tag{2.9}$$

$$-\frac{\hbar^2}{2m}\frac{d^2}{dz^2}\Psi_{RT} = E\Psi_{RT} \tag{2.10}$$

Defining a current density (flux) as:

$$j = \frac{\hbar^2}{2im}(\Psi^*\frac{\partial\Psi}{\partial z} - \frac{\partial\Psi^*}{\partial z}\Psi) \tag{2.11}$$

and understanding that $D = \frac{\Psi_{RT}}{\Psi_L}$, D can be solved as

$$D = \frac{(2\omega)^2 kq}{\omega^2(k+q)^2 + (\omega^2 + k^2)(\omega^2 + q^2)sinh\omega\alpha} \tag{2.12}$$

When this particular model is applied tunneling barriers, the barrier height is found to be on a similar order to the work function while the barrier width corresponds to the tip-sample distance. With similar work function values as the prior example, it is found that the sinh term in the equation dominates, leading to the following relation:

$$D \propto e^{-2\kappa z} \tag{2.13}$$

where

$$\kappa = \frac{\sqrt{2m(V_0 - E)}}{\hbar} \tag{2.14}$$

This is the decay constant for the exponentially decaying wave. In this case, the wavefunction for an electron is continuous and describes it penetrating through the barrier in the positive z direction. The probability for transmission through the barrier depends on the barrier width as described earlier. The challenge with this approach is that it does not consider the electronic structure of the surface or the tip, nor does it consider the shape of the potential barrier. As a result, a more accurate method is required and is developed in the Bardeen transfer Hamiltonian approach.

2.1.3 Bardeen Transfer Hamiltonian Approach

Bardeen's approach [28] to tunneling viewed the process as an effect of independent scattering events that transfer electrons across the potential barrier. Additionally, if the electronic states of the sample and the tip were known, it would be possible to resolve an expression for the tunneling current. This approach was based on the following set of assumptions [28][29]:

1. first order approximation for tunneling is valid due to tunneling being weak enough
2. the electronic states of the tip and sample remain unaffected despite being in the presence of the other
3. electron-electron interaction in the potential barrier is ignored
4. the occupation probabilities of electrons are independent of each other and constant
5. the tip and sample are in electrochemical equilibrium
6. the tip and sample atomic structures remain unperturbed

The following interpretation is based on the work of Gottlieb which refers to the Duke's interpretation of the Bardeen theory [29]. The result of ignoring the electron interaction in the potential barrier allows for the electrons to be described as a single-electron Hamiltonian:

$$-\frac{\hbar^2}{2m}\Delta\psi(r) + V(r)\psi(r) = H\psi \tag{2.15}$$

However, the challenges of resolving this single-electron Hamiltonian led to them being described independently in terms of their electronic states. As a result, it is possible to describe the system initially at t=0 as the tip and sample starting far apart, where there Hamiltonians are described independently in terms of an unperturbed tip or sample:

$$-\frac{\hbar^2}{2m}\Delta\psi(r) + V_S(r)\psi(r) = H_S\psi \tag{2.16}$$

$$-\frac{\hbar^2}{2m}\Delta\psi(r) + V_T(r)\psi(r) = H_T\psi \tag{2.17}$$

For the STM, it is separated into three sections: tip, barrier, and sample. The sample potential is equal to zero inside the tip potential and the tip potential is equal to zero in the sample potential. Both the tip and sample potential are equal to V(r) in their respective regions and inside the barrier.

If an electron starts initially with energy E in the sample state ψ and the wavefunction evolves from ψ at $t = 0$ to $\psi(t)$ at a time t, then $\psi(t) = e^{-itE/\hbar}\psi$. It is

assumed that the tip will approach the sample slowly and that the tip potential will be turned on adiabatically, as the time scale for sample approach is in seconds, while the tip potential is in femtoseconds. It is then possible to write $\psi(t)$ as:

$$\psi(t) = e^{-itE_s/\hbar}\psi + \sum a_k(t)\phi_k \tag{2.18}$$

where the the coefficients a_k will be approximated in order to determine the tunneling. The ϕ_k term refers to the bound states of tip Hamiltonian. It is important to consider the nomenclature here, where the wave functions correspond to stationary states being a solution only in tip or sample and what is valid for the entire system and under which Hamiltonian they yield which energy. This offers a different approach to the Bardeen paper, but perhaps gives further insight into the approach.

When inserted into the time-dependent Schrödinger equation $i\hbar\frac{\partial}{\partial t}\psi(r,t) = H\psi(r,t)$, the right-hand side gives:

$$\begin{aligned} H\psi(r,t) &= H(e^{-itE_s/\hbar}\psi) + \sum a_k(t)H\phi_k \\ &= e^{-itE_s/\hbar}E\psi + e^{-itE_s/\hbar}(H - H_S)\psi + \sum a_k(t)(E_k\phi_k + (H - H_T)\phi_k) \end{aligned} \tag{2.19}$$

and the left-hand side gives:

$$i\hbar\frac{\partial}{\partial t}\psi(r,t) = Ee^{-itE_s/\hbar}\psi + i\hbar\sum\frac{d}{dt}a_k(t)\phi_k) \tag{2.20}$$

Combining the two prior equations and taking the inner product of both sides in after canceling out common terms gives:

$$i\hbar\frac{d}{dt}a_j(t) = e^{-itE_s/\hbar}\langle\phi_j|H - H_S|\psi\rangle + E_j a_j(t) + \sum a_k(t)\langle\phi_j|H - H_T|\phi_k\rangle \tag{2.21}$$

Since the tunneling is considered weak in this system, the a_k term will be approximately zero based on our initial approximations. Further, by solving the system in terms of a_j with an initial condition of $a_j(t=0) = 0$,

$$|a_j(t)|^2 = \frac{4sin^2((E_{T,j} - E_S)t/2\hbar)}{(E_{T,j} - E_S)^2}|\langle\phi_j|H - H_S|\psi\rangle|^2 \tag{2.22}$$

At this point, the transmission probability $|\langle\phi_j|\psi(t)\rangle|^2$ still needs to be related to the $a_j(t)$ terms using equation (2.18). If assumed that $\langle\phi_j|\psi\rangle$ is small compared to $a_j(t)$, then $|a_j(t)|^2$ describes the transition probability. Thus, $\frac{d}{dt}\sum_j |a_j(t)|^2$ yields the tunneling rate where an electron initially in the sample state will transition into the tip state, which is approximately

$$\frac{d}{dt}\sum_k |a_k(t)|^2 = \frac{d}{dt}\sum\frac{4sin^2((E_{T,k} - E_S)t/2\hbar)}{(E_{T,k} - E_S)^2}|\langle\phi_k|H - H_S|\psi\rangle|^2 \tag{2.23}$$

Since this is based on an approximation where it is assumed that the states are orthogonal, even an exact solution to equation (2.21) will only yield an approximation

of the total scattering rate. This can be reduced further by Fermi's Golden Rule which is the general result of first order time-dependent perturbation theory. Defining $M^2(\phi,\psi) = |\langle\phi|H - H_S|\psi\rangle$ and $P_t(x) = sin^2(tx/2\hbar)/x^2$ and converting the sum in Eq. (2.23) into an integral, one receives:

$$\begin{aligned}\frac{d}{dt}\sum_k |a_k(t)|^2 &\approx \frac{d}{dt}4[M^2(\psi)\rho_T(E_S)\int P_t(E)dE] \\ &= \frac{d}{dt}4[M^2(\psi)\rho_T(E_S)\frac{\pi t}{2\hbar}] \quad \text{with}\end{aligned} \tag{2.24}$$

where $M^2 = \frac{1}{N_{E_S}}\sum_{k:|E_{T,k}-E_S|<2\hbar/t} M^2(\phi_k,\psi)$, N_{E_S} is the number of tip states, and $\rho_T(E)$ is the tip LDOS. The matrix elements of the sample state ψ_n can be approximated. This is derived from the way that Bardeen selected the potentials. Through a series of integration steps, it is found that the integral of $H - H_T$ in regards to the tip area is zero. Additionally, it is also found that integrating the matrix elements on the sample side is also zero. It is then possible to approximate the matrix elements $M = \langle\phi_j|H - H_S|\psi\rangle$ for the sample state at the energy of the tip, giving

$$\langle\phi_j|H - H_S|\psi_n\rangle \approx -\frac{\hbar^2}{2m}\int(\phi_j^*(r)\Delta\psi_n(r) - \psi_n(r)\Delta\phi_j^*(r))dr \tag{2.25}$$

Applying Gauss' theorem, the previous equation then reduces to Bardeen's approximation of the matrix element

$$M = -\frac{\hbar^2}{2m}\int_{surf}(\psi_n^*\nabla\phi_j - \phi_j\nabla\psi_n^*)d\mathbf{n} \tag{2.26}$$

As a result, this shows that rather than having to integrate over the entire region of the tip-barrier, taking the surface integral of the barrier is a sufficient approximation.

2.1.4 Tersoff-Hamann Approximation

After the invention of the STM, Tersoff and Hamann [30] built on the Bardeeen approach by combining the method with an s-type tip wave function which is radially symmetric. One of the motivations was the difficulty to determine the tip states. The STM tunneling current is a convolution of the tip and sample states, so a new model was proposed that simplifies the tip states in order for them to be removed and model the tip as a point. For the interpretation of large STM image features, the TH model performs well, but breaks down when it predicts atomic scale resolution features beyond the detection limit of the STM.

The matrix elements in Eq.2.26 were found by Tersoff and Hamann [30] to reduce to the following relation:

$$I \approx \sum_v \psi_n(r)\delta(E - E_F) = \rho_s(r, E_F) \tag{2.27}$$

This can be interpreted that the STM measures the tunneling current which is proportional to the Local Density of States (LDOS) at a given position of the STM tip. Despite this development, the relation is still limited by a series of assumptions including:

- Low temperature
- Low bias voltage (up to 10mV)
- S-wave tip
- Uniform density of states at the Fermi energy

While the assumptions are limiting, they do provide a reasonably accurate model for the STM data. In practice, the low temperature value is often not satisfied, in addition to the tip, which are typically made from transition metals, where the d-wave features cannot be ignored. In order to move beyond these limitations, another model was proposed, called the WKB model [31], which is a semi-empirical approach. The model predict the tunneling current as

$$I(V,d,r) = \int_{-\infty}^{\infty} d\epsilon \rho_s(\epsilon,r)\tau(\epsilon,V,d)[f(T_s,\epsilon-eV) - f(T_t,\epsilon)] \tag{2.28}$$

with

$$\tau(\epsilon,V,d) = exp[-2d\frac{\sqrt{2m}}{\hbar}\sqrt{\frac{\Phi_s+\Phi_t}{2}+\frac{eV}{2}-\epsilon}] \tag{2.29}$$

representing the tunneling transmission probability of a single electron at a defined bias voltage and energy. $d\epsilon\rho_s(\epsilon,r)$ is defined as the as the LDOS of the combined tip and sample, while the T_s and T_t are the temperatures of the sample and tip respectively.

From Eq.2.1.4, it is shown that the LDOS and the tunneling current are proportional. For zero voltage bias, the tunneling current is also zero as a result of the Fermi levels being equivalent in both the tip and the sample. It can also be shown that the tunneling current is dependent on the density of the unoccupied states of the sample. For example, for an applied positive bias voltage on the sample with respect to the tip, electrons can tunnel into states above the Fermi energy.

Another interesting property of STM is the differential conductance. For instance, $f(\epsilon)$ becomes a step function at the low temperature limit, which allows for a simplification of Eq.2.1.4 to the following relation for the differential conductance

$$\begin{aligned}\frac{dI}{dV}(V,d,r) = \quad & \rho_s(E_F+eV,r)\rho_t(E_F,r)\tau(eV,eV,d) \\ & + \textstyle\int_{E_F}^{E_F+eV} d\epsilon\rho_s(\epsilon,r)\rho_t(\epsilon-eV,r)\frac{\delta}{\delta V}\tau(\epsilon,eV,d)\end{aligned} \tag{2.30}$$

When the voltage bias is low, then the transmission probability will be a smooth and varying function. This results in a smooth background where the $\frac{\delta\tau}{\delta V}$ can be ignored and the following simplification made:

$$\frac{dI}{dV} = \rho_s(E_F+eV,r) \tag{2.31}$$

which directly relates the data of a $\frac{dI}{dV}$ to the DOS as a function of energy at a particular point. The challenge with the Bardeen approach was due to the tip states. The imaging method of an STM relies upon the convolution of the electronic state of the tip and the sample. Tersoff and Hamann proposed that by simplifying the tip properties, it can be factored out of the calculation, allowing the STM image to be related to the intrinsic surface properties, rather than a convolution of the tip and sample properties. In the next section, this oscillating system will be discussed in the context of measuring the forces between a tip and a sample.

2.2 Introduction to Atomic Force Microscopy

This chapter reviews over the basics of atomic force microscopy. Section 2.2.1 provides a background on the principles of operation. Section 2.2.2 explains different types of AFM modes. Section 2.2.3 addresses the forces involved in AFM. Section 2.2.4 introduces the reader to the quartz tuning fork used in experimental studies. Section 2.2.5 reviews over the AFM feedback loops. Section 2.2.6 reviews over tip modification methods and carbon monoxide tips.

While the sharpness of an STM tip and the subsequent tunneling through the final atom yield high resolution images, one of the limitations of STM is the need for conductive samples or ultra-thin insulators on metals. The AFM builds upon the advancements made by the STM, offering both similar equipment and techniques, but instead operates by measuring the forces acting on a sharp tip rather than the current. Invented by Binning et al. in 1986 [32], the AFM has been capable of resolving true atomic resolution, mapping insulators, and providing a way of mechanically manipulating atoms [33] [34] [21]. Additionally, AFM is sensitive to chemical interactions and short-range forces between the oscillating tip and surface. As a result, detailed images and spectroscopy can be performed on atoms and molecules on a surface. Additionally, the AFM is sensitive to electrostatic, magnetic, and long-range van der Waals forces. Initially, AFM was performed in contact with the sample, but newer methods allow for non-destructive and non-contact methods to map the sample, while measuring the tip-sample interaction.

With AFM, the atomically sharp tip mounted on a cantilever is scanned across a surface while the cantilever is deflected by the tip-sample interaction. Originally, this deflection was measured using a secondary STM [32], but was eventually replaced by optical (Fig 2.4 (a)) and capacitive methods for detection.

The sensitivity and resolution of the measurements are determined by a few primary parameters of the cantilever: the spring constant k, the quality factor Q, and the eigenfrequency f_0. In order to ensure sufficient sensitivity for short range forces, a sensor of stiff piezoelectric material, quartz, is excited at sub-nanometer amplitudes. Many AFM experiments operate with silicon cantilevers (Fig. 2.4) with optical beam deflection that can be operated at sub-nm amplitudes with atomic resolution. A more modern development is the qPlus force sensor, developed by Giessibl in 2000 [35], which is more commonly found in operation at UHV and low-temperature environments. Originally developed from ordinary quartz tuning forks as used in

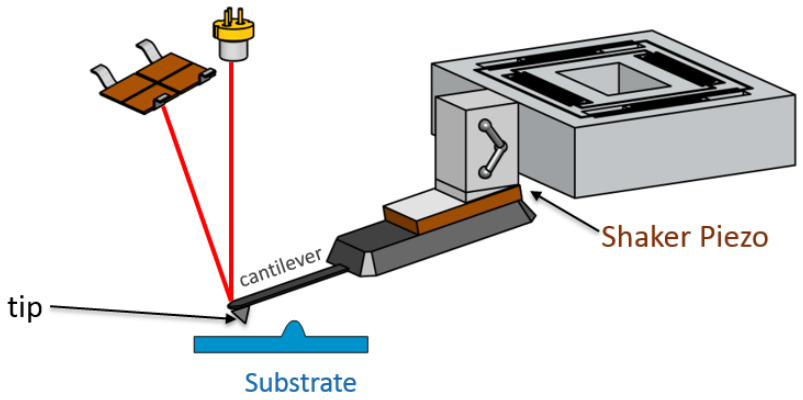

(a)

Figure 2.4: (a) AFM silicon cantilever tip with optical beam deflection measurement. Reprinted with permission from Nanosurf AG.

inexpensive wrist watches, the tuning fork is installed with one arm secured to a mounting plate while the other arm is affixed with a tip and is free to oscillate. The advantage of the qPlus over previous attempts to use quartz tuning forks was that only one prong oscillates instead of both, which allows for similar operation compared to a standard silicon cantilever, greatly simplifying image interpretation and theoretical modeling. In ambient and low temperature environments, the sensors have the ability to detect long-range forces and achieve atomic resolution, in addition to atomic manipulation and imaging of the charge state [36] [37].

The versatility of the AFM allows it to function in static or dynamic mode. The static operating mode relies upon the deflection of the cantilever when brought close to the surface. The deflection of the cantilever corresponds directly to the tip-sample interaction by the cantilever spring constant. Since the tip is operating close to the sample, there is the risk of sample damage by a tip-sample collision should the restoring force not be sufficient. In dynamic mode, the repulsive forces are measured while being brought in contact with the sample. Previously, dynamic mode used to measure the attractive forces during oscillation and had issues with the snap-to-contact, resulting in further tip-sample distances or lower amplitude values. With the development of the qPlus force sensor, its high stiffness value allows it to probe the repulsive forces and remain at small tip-sample distances.

In the dynamic mode, the cantilever is oscillated at or near its resonance frequency f_0. The cantilever and tip then are brought close to the sample, where the resonance frequency will change to a new frequency $f_0 + \Delta f$. The tip-sample interaction is then detected using either amplitude modulation (AM) or frequency modulation (FM) forms of AFM. In amplitude modulation AFM (AM-AFM), the cantilever excitation is set close to resonance frequency with a constant amplitude and then the phase between the excitation signal and the cantilever oscillation as well as the amplitude of the cantilever's oscillation will be related to changes in the force gradient. In this mode, the topography traced along the surface originates from constant amplitude contours. The changes are dependent on the time scales at which

these changes occur [38], which results in a decrease in acquisition speeds in UHV. This was improved upon in frequency modulation AFM (FM-AFM), which allows for detailed quantitative force measurements and will be used throughout this work.

2.2.1 Principles of Operation

In AFM, the imaging signal is derived from a force which acts on the AFM tip and the oscillatory frequency of the cantilever. The periodic motion of the cantilever can be treated as a harmonic oscillator with one degree of freedom. In an unperturbed system, this can be treated as a $q(t) = Acos(2\pi f_0 t)$, where f_0 is the resonance frequency. $f_0 = \frac{1}{2\pi}\sqrt{\frac{k}{m}}$ where m is the effective mass of the cantilever and k is the spring constant. By introducing a force between the sample and the tip, the effective spring constant changes by $k* = k - \partial F/\partial z$, where z is the separation between the tip and the sample. If the gradient of the force is assumed to be small compared to k, the frequency shift is defined as:

$$\frac{\partial f}{f_0} = \frac{f - f_0}{f_0} = \frac{1}{2\pi f_0}(\sqrt{\frac{k*}{m}}\sqrt{\frac{k}{m}}) \approx \frac{1}{2k}\frac{\partial F}{\partial z} \tag{2.32}$$

This approximation is only valid for small amplitudes in comparison of the decay length of the force. At small oscillation amplitudes, this approximation is sufficient to relate the frequency shift to the force gradient. If k is roughly constant over one oscillation cycle, particularly when probing repulsive interactions, then this criterion will not be valid anymore. A more general description of these oscillation amplitudes is described by [39]. The frequency shift can be described more generally by the Hamilton-Jacobi approach, which developed from first-order perturbation theory [40]

$$\Delta f = -\frac{f_0^2}{kA}\int_0^{1/f_0} F(z + A[1 + cos(2\pi f_0 t)])cos(2\pi f_0 t)dt \tag{2.33}$$

$$\Delta f = -\frac{f_0}{\pi kA}\int_{-1}^{1} F(z + A[1 + u])\frac{u}{\sqrt{1 - u^2}}du \tag{2.34}$$

Should the F(z) value be known, this equation can be used to calculate the frequency shift. This F(z) value is often experimentally derived as an analytic solution to the equation is not known. Another approach to solving this equation was developed by Sader and Jarvis [41], which provides results over different amplitude situations. In the Sader-Jarvis method, the force is expressed in terms of the frequency shift with a Laplace and inverse Laplace transform

$$F(z) = \mathcal{L}[\frac{kA}{T(\lambda A)}\mathcal{L}^-1[\frac{\Delta f(z)}{f_0}]] \tag{2.35}$$

where $T(x) = I_1(x)exp(-x)$ where I_1 is a modified Bessel function. By using the following approximation of T

$$T(x) \approx \frac{x}{2}(1 + \frac{1}{8}\sqrt{x} + \sqrt{\frac{\pi}{2}x^{3/2}})^{-1} \tag{2.36}$$

it is then possible to find the expression describing the force

$$T(x) = \frac{2k}{f_0}\int [1 + \frac{\sqrt{A}}{8\sqrt{\pi(t-z)}}]\Delta f(t) - \frac{A^{3/2}}{\sqrt{2(t-z)}}\frac{\partial \Delta f(t)}{\partial t}dt \tag{2.37}$$

The Sader-Jarvis method has been shown to be accurate with deviations from the actual force law of less than 5 percent [41].

2.2.2 Amplitude and Frequency Modulation

Numerous methods of AFM operation exist, but the two general operating modes of AFM are contact mode and non-contact mode AFM. In contact mode, the tip is brought down in mechanical contact with the sample surface. Mechanical contact, in this case, refers to tip being brought to the repulsive regime. The tip is then raster-scanned across the sample surface and the repulsive interaction being measured. Non-contact mode AFM, which is the method that will be the only one discussed later, operates at larger separation distances between the tip and sample. The tip is dynamically oscillated close to the surface and depending on the precise tip-sample distance, either short- or long-range forces will dominate the image contrast. Unlike contact AFM, the non-contact oscillatory motion is performed at distances that will ensure that the tip is not irrecoverably damaged. The oscillations of the cantilever are measured and the amplitude, frequency and phase of each oscillation can be recorded.

Present methods of AFM primarily utilize FM-AFM for experiments performed under ultra-high vacuum (UHV) conditions and at low temperatures. In FM-AFM, the cantilever is oscillated at its resonance frequency. Tip-sample interactions induce a shift in the resonance frequency, which can be measured to generate a real-space image of the surface. This frequency shift depends on the tip-sample separation and under certain conditions, is approximately proportional to the vertical gradient of the tip-sample forces. The frequency shift can be used to generate a real-space image of the surface.

Unlike in contact mode, measurements occur further above the surface with the oscillations of the cantilever allowing the tip to penetrate into the short-range regime at only the closest approach point and only with the last few atoms of the tip apex. The advantage is that this allows the tip is only within this regime for a brief part of the entire oscillation period, reducing the possibility of unintended tip-sample interaction. Both FM-AFM and AM-AFM can operate in both repulsive and attractive regimes depending on the defined setpoints [42][43]. Repeated oscillations will result in an amplitude reduction and requires additional input in order to maintain a constant amplitude. Additionally, it is not possible to utilize the AM-AFM method for atomic scale resolution in UHV, as the bandwidth limitations at higher Q values result in delayed signal collection [43].

2.2.3 Short-Range and Long-Range Forces

In STM, the tunneling current is a monotonic function of the tip-sample distance, where the probability of an electron tunneling across the vacuum barrier decays exponentially. This is not the case with AFM, where the total tip-sample force is dependent on the relative contribution of the various forces which changes with distances. In a simplified view, attractive van der Waals forces dominate at further distances, while chemical forces dominate in the short-range and are repulsive. This interaction range directly influences the achievable spatial resolution.

Despite this, the forces are not exclusively equal. For example, the two most prominent model potential for interatomic short-range forces are the Lennard-Jones potential and the Morse potential. Both potentials consist of attractive and repulsive terms, but in the Lennard-Jones potential, the attractive term is a $-1/r^6$ two-atom like London dispersion, where there is no wave function overlap but instead instantaneous multipoles) and the repulsive term is a $1/r^{12}$ term accounting for Pauli repulsion, where there is wave function overlap. The Lennard-Jones potential does not describe the chemical bonds, as it the description is too weak, but instead describes the interaction between two inert noble gas atoms. For our experiments, it can describe the interaction between a functionalized CO tip and a sample. The Morse potential is a sum of exponential terms, describing covalent bonding in a diatomic molecule and accounting for chemical interactions.

van der Waals

Long range interactions are those forces that can occur at distances up to several nanometers. However, over a long distance, the interaction can occur between several atoms on the surface and the tip, resulting in a degraded image of the surface as the atomic structure becomes obscured. The AFM can detect these long-range forces, such as the van der Waals (vdW) forces, which allow for the non-contact mapping of a surface. The primary contributions of intermolecular van der Waals forces are:

- Keesom (orientation) forces between two permanent dipoles
- Debye (induction) forces between an induced dipole and a permanent dipole
- London (dispersion) forces between two induced dipoles

In UHV conditions, the vdW interaction is always positive, but can be made repulsive by the selection of a separation medium. While the interaction energy may seem to become small compared to the strength of the covalent bonds, the vdW force is a cumulative effect. It is found that the relation for the potential energy between two atoms and the distance is:

$$U_{vdW} \propto \frac{1}{z^6} \tag{2.38}$$

Approximating the macroscopic van der Waals force can be done by modeling the system as a spherical tip of radius r close to the surface and a semi-infinite flat plane for the surface. Rather than a discrete summation of the interactions of pairs of atoms, integration can be used to reduce the calculations based on the following assumptions:

1. continuous medium of constant density,

2. constant material properties over the integration volume.

The force then becomes

$$F_{vdW} = -\frac{Hr}{6z^2} \tag{2.39}$$

where H refers to the Hamaker constant, which is dependent upon the sample and tip materials and calculated for a variety of materials. Atomic resolution imaging requires a reduction of the long-range interaction effects, since the vdW force is always occurring between sample and the tip. In UHV, the usage of atomically sharp tips with high aspect ratios is desirable as the vdW force is reduced due to the smaller integration volume. The tip apex will have a single atom, but the influence of additional nearby atoms at the tip apex can impact the image contrast and resolution.

Electrostatic

An electrostatic force is defined as the attraction or repulsion of charged particles. Charging can have a strong impact on the contrast of the images produced by AFM [44]. Should a sample be cleaved or cleaned, the surface of the sample can remain in a charged state. Annealing the crystal before inspection can cause any charges to diffuse into the system, eliminating the issue.

Of more importance in this thesis is the potential difference between an AFM tip and a sample. These two, when brought close together, form a capacitor where the energy stored is:

$$E = -\frac{1}{2}C(V_{TS} - V_{LCPD})^2 \tag{2.40}$$

where V_{TS} is the applied voltage between the tip and the sample, C is the capacitance between the tip and sample, V_{LCPD} is the contact potential difference between tip and sample. This means that the even at zero applied bias, a potential difference may be present across the SPM junction. Not only does V_{LCPD} contain the difference in work function, but it also contains the contributions from the dipoles and charges . This results in the following electrostatic force:

$$F_{elec} = -\langle\frac{\partial E}{\partial z}\rangle = \frac{1}{2}\langle\frac{\partial C}{\partial z}\rangle(V_{TS} - V_{LCPD})^2 \tag{2.41}$$

that is an attractive force. This relation is used later for Kelvin probe force microscopy.

Chemical Forces

These forces originate from the formation and breaking of chemical bonds between the sample surface and tip. Due to the limited interaction outside of the electron orbitals, this force primarily occurs between the nearest surface atom and the tip apex. Both attractive and repulsive, the force is driven primarily by the type of the interacting atoms. As the atoms are brought closer together, the valence orbitals begin to be filled and gradually pushed to the molecular orbitals which then creates an attractive force which only continues to bring the atoms together.

Despite the attractive component following the distance dependence in Eq.(2.39), the repulsive component has no universal distance dependency. The repulsive force originates from the Pauli exclusion principle and nuclei repulsion. While difficult to

predict how this interaction force behaves, there are several approximation methods that describe the chemical interaction including: the Lennard-Jones potential and the Morse potential. It should be noted that these two methods do not solve the formation or breaking of bonds, but can provide insights to them and can be solved analytically.

The Lennard-Jones (LJ) potential [45] is used due to the simplicity in theoretical calculations:

$$U_{LJ} = U_0\Big[\Big(\frac{z_0}{z}\Big)^{12} - 2\Big(\frac{z_0}{z}\Big)^{6}\Big] \tag{2.42}$$

where z_0 is the equilibrium distance and U_0 is the energy at z_0. The resulting force of the LJ potential is

$$F_{LJ} = \frac{12U_0}{z_0}\Big[\Big(\frac{z_0}{z}\Big)^{13} - \Big(\frac{z_0}{z}\Big)^{7}\Big] \tag{2.43}$$

Another method to model the interaction energy is to utilize an exponential distance dependence. Referring back to the theory in STM, the electron wave function in a vacuum decays exponentially, justifying the relation for the repulsive component. The Morse potential [46] builds upon this relation by applying the exponential distance dependence to both the attractive and repulsive components

$$U_{Morse} = 2U_0(1 - e^{-2\beta(z-z_0)}) \tag{2.44}$$

where β is the decay constant. The Morse potential describes the chemical bond with the bond energy U_0. Careful selection of the bond energy, decay constant values, and distance allow it to be used to model chemical bonds for $H_2{}^+$. The Lennard-Jones potential does not show good agreement with metallic surfaces while the Morse potential is anisotropy in chemical bonds. Despite their usage, neither potential accurately describes the Pauli repulsion, but they can be used to qualitatively describe the distance dependence of the tip-sample interaction.

2.2.4 Quartz Tuning Fork

The usage of quartz tuning forks (QTF) in scanning probe microscopy originated from work in acoustic near field microscopy [47], where it detected the decrease in resonance frequency and amplitude caused by hydrodynamic forces. Further advances were made by Edwards et al. in 1997 where a quartz tuning fork was utilized as an AFM cantilever, where both the prongs of the fork oscillated freely [48]. The challenge with this setup was the asymmetry introduced by having a tip affixed to one of the prongs, whereas the qPlus solution developed by Giessibl fixed one of the prongs [49], allowing for the signals collected to be more easily interpreted. Fig 2.5 (a) shows an example of a typical QTF used in AFM experiments. Fig 2.5 (b) shows a schematic of a nc-AFM QTF assembly with attached tip.

The quartz tuning fork is not a device novel to SPM, but is commonly found in various watches and other time sensitive equipment. To ensure that only antisymmetric oscillation modes in-plane are possible, the electrodes of each opposite face on a single prong are connected, while the prongs themselves are connected in the reverse.

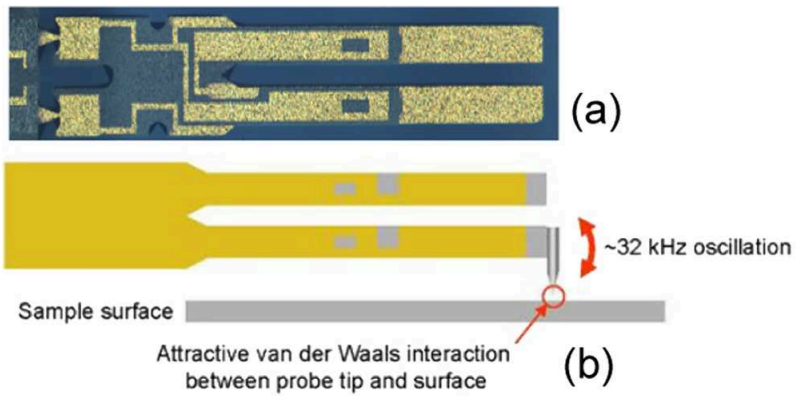

(a)

Figure 2.5: (a) Optical micrograph of a QTF. (b) Schematic diagram of a typical nc-AFM QTF with attached tip. Reprinted with permission from [50].

QTFs are defined primarily by two properties: the stiffness and the quality factor or Q-factor. A common value for the stiffness is 1800 N/m [35], which allows for small oscillation amplitudes of <1 nm. The Q-factor represents the stability of oscillation, which is connected to the number of cycles the fork has oscillated before the amplitude has decreased to A/e. A high Q-factor, as seen in nc-AFM operated in UHV conditions, ensures a more accurate measure of the frequency shift and minimal heat dissipation. The small oscillation amplitudes and high Q-factor allow for measurement of not just the forces, but also the tunneling current.

2.2.5 Feedback loops

The feedback loop is the critical component to controlling the tip-sample distance in scanning probe microscopy. For AFM, high-resolution imaging and force spectroscopy is achievable through measurement of the sensor's frequency shift. By determining the resonance frequency of the tip by moving far away from the sample, it is then possible to compare the perturbed measured signal against the established unperturbed resonance signal. In AFM, this is addressed by the phase-locked loop (PLL).

The PLL adjusts the phase and the frequency of a voltage controlled oscillator (VCO) to match the signal of the reference oscillator. Initially, the phase difference is zero, as the system will be synchronized, but as the system output changes, the PLL will readjust the VCO until the phase difference is minimized or close to zero. The output of the PLL is a DC voltage signal which is proportional to the frequency shift of the QTF. Additionally, in comparison to STM, (FM) nc-AFM requires two additional feedback loops for the frequency shift as well as the amplitude regulation. STM operates only on a tip-height feedback loop.

2.2.6 Tip Functionalization

Achieving suitable contrast and resolution necessitates more than just an atomically sharp tip to view the chemical structures of individual molecules. The reasoning is

due to the fact that metallic tips are reactive, interacting strongly with the surface. Additionally, molecules are manipulated or picked up before the tip-sample distances are small enough for atomic resolution. Through a tip functionalization process, it is possible to achieve atomic scale contrast [34]. The Pauli exclusion principle is the basis for submolecular contrast and can be verified with density functional theory (DFT) calculations [51], but this depends upon the tip-sample distance being quite small and the tip termination being chemically inert. This also allows for the study of molecules adsorbed onto surfaces due to the single pair of electrons of the oxygen atom at the end of the tip being unable to form covalent bonds [52].

In this thesis, a single CO molecule was selected as the tip termination, but others, such as pentacene, a single Xe atom, or a Cl atom are also possible[51]. The selection of the CO molecule was due to the ease of tip and sample preparation as well as the image quality, with established methods for both. The high resolution of the AFM images with a CO molecule are determined is due to the strongly localized wave function of the CO molecule [51] in addition to tip flexibility [53].

For STM, there is a distinct change in the images generated, particularly the contrast, with a CO tip compared to a metal terminated tip. With a metal tip, the s-wave states dominate further into the vacuum, while with a CO-terminated tip, the π orbitals represent the p-wave tip states [30] [54] While not all metal tips are well-described by s-wave tips. From the Tersoff-Hamann analysis, s-wave tips should not be able to yield atomic scale resolution on close-packed metal surfaces. In those cases, the metal tip potentially has a strong d-wave character. The tunneling matrix elements of p-wave tips are proportional to the derivative of the LDOS [25] [27]:

$$M_{P_x} \propto \frac{\partial \Psi}{\partial x} \tag{2.45}$$

$$M_{P_y} \propto \frac{\partial \Psi}{\partial y} \tag{2.46}$$

2.3 Introduction to Kelvin Probe Force Microscopy

This chapter addresses the basics of Kelvin probe force microscopy. Section 2.3.1 discusses the theoretical background of KPFM.

The design and performance of nanoelectronic devices, including present and future designs, depends on the properties of molecular junctions at a scale of only a few nanometers. Various methods exist to characterize these properties, but only one will be discussed at length: Kelvin probe force microscopy.

KPFM is a method where the local electrostatic potentials of a sample can be measured with an AFM, similar in principle to a macroscopic Kelvin probe. Another method, Electrostatic Force Microscopy (EFM), measures the force produced on a charged tip based upon the surface electric field. KPFM minimizes the electrostatic forces by adjusting the bias voltage between the tip and the sample. This allows KPFM to then directly measure the contact potential difference (CPD) between the tip and the sample, which contains contributions from the work function between the tip and the sample structures as well as other contributions such charges trapped in the structures.

KPFM is used to determine the nanoscale electronic properties of various metal-semiconductor surfaces and organic and semiconductor devices. It provides a unique way of gathering information on electronic properties that would otherwise be unobtainable.

2.3.1 Principles of Operation

KPFM originates from observations and measurements by William Thomson, Lord Kelvin, during an experiment of two electrically charged plates that were separated by a small distance, forming a capacitor. The potential difference in this experiment originates from the difference in the work function of the two plates. The technique was implemented by Nonnenbacher et al. [55] in order to measure the local contact potential difference (CPD) using AFM.

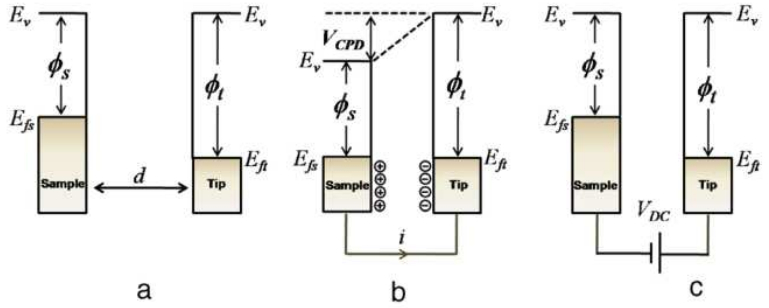

(a)

Figure 2.6: Electronic energy levels of the tip and sample: (a) tip and sample are separated by distance d with no electrical contact, (b) tip and sample are in electrical contact, and (c) external bias is applied between tip and sample to nullify the CPD/tip–sample electrical force. Reprinted with permission from [56].

Similar to Kelvin's macroscopic experiment, in KPFM, the tip and the sample form a microscopic capacitor as seen in Fig 2.6 (a). The energy stored in the capacitor is given by Eq. (2.40):

$$E = \frac{1}{2}C(V_{TS} - V_{LCPD})^2$$

where KPFM measures a CPD between the conducting tip and the sample. Both the tip and the sample will have differing work functions, which is the difference between the Fermi and the vacuum levels for each material (Fig 2.6 (b)). The difference in work functions is defined as the CPD (V_{LCPD}) The physics of KPFM can be understood as the following: If two metals with different work functions are not in contact, the vacuum level is the common reference, i.e. they will be the same for both metals and their Fermi levels will be at different energies. Once the metals are brought into contact, their Fermi levels will align, as the electrons all need to have the same chemical potential to reach an equilibrium. This means that electrons will flow from the metal with the lower work function the metal with the higher work function until their Fermi levels are aligned. This redistribution of electrons

gives rise to an electric field and thus the contact potential difference. This field is compensated for in KPFM by adjusting the tip-sample voltage (Fig 2.6 (c)). The electrostatic force F_{elec} is then given by Eq. (2.41):

$$F_{elec} = -\langle \frac{\partial E}{\partial z} \rangle = \frac{1}{2} \langle \frac{\partial C}{\partial z} \rangle (V_{TS} - V_{LCPD})^2$$

In KPFM, only the electrostatic forces are dependent on the bias voltage, allowing the detection of their contribution to the measured frequency shift. Any modulation of V_{TS} will cause a modulation in F_{elec} and it is thus possible to compensate for the contribution of the electrostatic force by modifying the bias voltage until the frequency shift for a particular height is minimized.

In the frequency modulated detection scheme, the PLL is tracking the frequency of the cantilever. The frequency shift output signal contains a electrostatic modulation frequency, which is then filtered out in the feedback loop. This method then generates a potentials map that shows where the electrostatic force gradient is minimized, which is proportional to the frequency shift and written as:

$$k_{TS}^{elec} = \langle \frac{\partial F_{elec}}{\partial z} \rangle = \frac{1}{2} \langle \frac{\partial^2 C}{\partial z^2} \rangle (U_T S - U_{LCPD})^2 \tag{2.47}$$

In present experiments, a grid of point spectroscopy, where the frequency shift is measured as a function of the bias. Then, these values are fit to a second-order polynomial to determine the voltage at which the frequency shift is minimal.

3 Experimental Setup

3.1 Createc STM/AFM Microscope

The work carried out in this thesis was performed on a commercial UHV low-temperature scanning tunneling microscope (LT-STM) from Createc. The system has undergone some additions and modifications since its initial installation, some of which I have assisted with to help improve its performance. The following sections describe the equipment setup, software to control the system, and some of the challenges encountered when using the system.

The Createc LT-STM consists of two interconnected chambers separated by a gate valve, one for sample preparation and the other for the STM. The entire system is decoupled from the floor by four pneumatically damped feet in order to reduce vibrational noise and provide system stability.

The preparation chamber consists of a manipulator arm, an evaporator, an ion-bombardment sputtering gun, a quadropol mass spectrometer (QMS), and an ion gauge. The STM chamber consists of an STM head and a liquid helium bath cryostat, consisting of a liquid helium dewar surrounded by a liquid nitrogen dewar. Samples and tools are transferred between chambers by the manipulator arm and can be used to transfer the sample in and out of the STM head. The manipulator arm is used for positioning samples in front of the sputtering gun and evaporator. It also functions as a heating and cooling mechanism for samples.

Both chambers are connected to a gas insertion system, which allows for multiple purified gases to be dosed into the system through leak valves via either the sample preparation chamber or the sample analysis chamber. The sputtering gun connected to the preparation chamber is supplied with neon gas via the gas insertion system. A mass spectrometer is also attached the system in order to measure the different gases in the vacuum.

Evaporation of organic molecules can be performed with a commercially available Createc Triple Turbo Micro Effusion Cell with three independent crucibles. The flux is controlled via a shutter in front of the crucibles, with the potential to use multiple crucibles simultaneously. An additional home-made, double-crucible evaporator is installed in the load-lock that allows for individual crucible temperature control.

Samples and tools are initially loaded from the ambient environment by means of a turbo molecular pumped load-lock connected to the sample preparation chamber via a gate valve. The turbo molecular pump (Pfeiffer) is connected to a rotary vane pump (Pfeiffer) for pump down operation. Multiple samples can be stored in the STM chamber at UHV in the sample storage rack while additional tools, STM tips, and qPlus sensors can be stored on the manipulator arm. Due to the vibrational noise, the turbo molecular pump can be switched off to improve the quality of the STM images.

The UHV system is maintained by two Gamma Vacuum ion getter pumps with titanium sublimation pumps (TSP) connected to the sample preparation and STM chambers. This results in a base pressure of low 10^{-10} mbar throughout the system. The advantage of the design of this system is that samples, tips, and other tooling

can be changed in situ without needing to breach the UHV environment in either chamber.

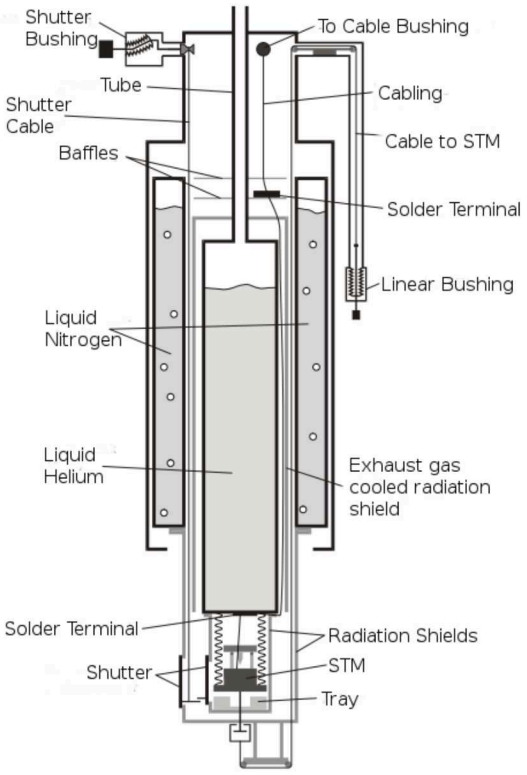

(a)

Figure 3.1: (a) 2D diagram of Createc STM chamber. Adapted from CreaTec Fischer and Co. GmbH.

The STM chamber contains a liquid nitrogen and liquid helium cryostat as shown in 3.1 (a). The STM head is attached to the liquid helium cryostat by three springs, allowing the STM to reach temperatures as low as 4.2 K. Radiation shields surround the STM head, which allow the STM to reach the low temperatures. The inner shield of is connected to the liquid helium dewar and surrounded by an outer shield which is at liquid nitrogen temperatures. For instances such as sample transfers, cooling down the STM head requires the use of a clamping mechanism, which fixes the STM head to the inner liquid helium shield. During normal scanning operation, there is sufficient cooling power to allow the STM head to remain unclamped. This clamping process is also used to facilitate the transfer of samples into and out of the STM head. Additionally, the three springs in the STM head vibrationally decouple from the surrounding chamber during measurements. Finally, the STM head and inner liquid helium shield contain magnets to help isolate the system through an eddy current damping system to further prevent mechanical noise.

Fig 3.2 (a) shows the STM/AFM microscope, with the sample below the mounted qPlus sensor and tip. In Fig 3.2 (b), the qplus sensor can be seen, consisting of the quartz tuning fork and tip mounted on the free end. The STM/AFM microscope

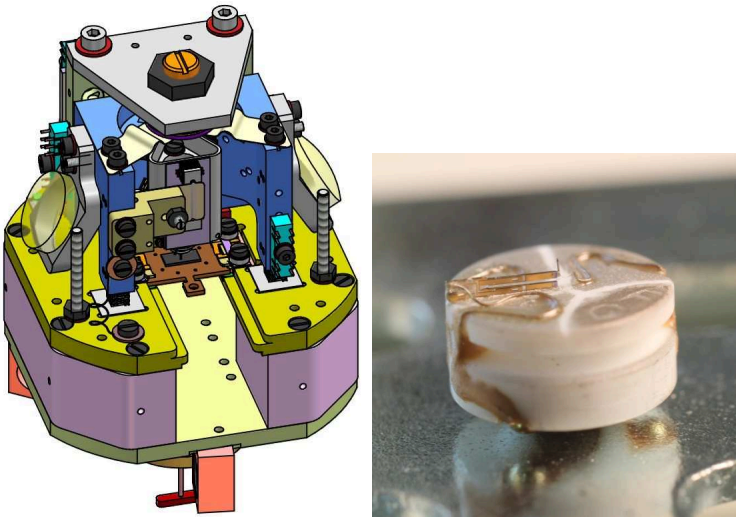

(a) (b)

Figure 3.2: (a) 3D model of Pan-style slider STM microscope with sample plate mounted. Reprinted with permission from CreaTec Fischer and Co. GmbH. (b) qPlus force sensor.

is a Pan slider-style scanner consisting of a sapphire prism onto which a tube-piezo scanner is attached. The Z-motion is linear on the sapphire prism, while the XY coarse movement is provided by a separate set of shear piezos. At the end of the tube scanner, a small ring piezo is mounted for excitation of the tuning fork. During scanning operation, the entire system hangs free on a set of metal springs. These springs function to isolate the system from external vibrations such as pump noise, acoustic noise, or building noise.

3.2 Electronics

In order to amplify the signal from the STM microscope, the system is equipped with an external preamplifier (FEMTO DLPCA-200). The STM can also be amplified by an internal preamplifier with a gain of 10. The AFM signal is amplified first by an internal preamplifier but does not pass through the FEMTO. Additionally, the system also is equipped with an external phase-locked loop (PLL) detector (Nanonis OC4) which is used to detect the frequency shift and keep the amplitude constant. The major electronic components of the system include:

1. High-Voltage (HV) Generator
2. Digital Signal Processor (DSP)
3. External PLL
4. Lock-in Amplifier

Other electronics, such as the preamplifier, while important, do not warrant further discussion. Starting from the PLL, a setpoint amplitude A is established by

the user. The PLL reads the piezo signal from the qPlus tuning fork and extracts the amplitude A and frequency shift Δf. Then, the PLL calculates the necessary excitation signal EXC that will allow the amplitude A to remain constant. The excitation signal goes directly to the scanner and is sent to the DSP for recording. The frequency shift is also sent to the DSP, where it can be used as a feedback parameter for height. If not used, the user-established tunneling current I can be used as a feedback parameter. Both feedback parameters, regardless of which is used, are used to control the tip-sample distance via the HV generator. During a scanning operation, the X and Y piezo will also be controlled by the DSP. Additional information is obtained via the lock-in amplifier, which is used to modulate the sample bias and measure the dI/dV by the response of the tunneling current.

3.3 Sample Preparation

The experiments were performed on clean single crystal copper, which were cleaned inside the prep chamber with multiple sputtering and annealing cycles. Ne^+ sputtering was performed at an ion energy of approximately 1 keV for 20 minutes. Annealing temperatures were set and held at 650°C, as measured by a pyrometer, for 5 minutes.

Cu(111) is a close-packed surface with an interatomic distance of 2.55 Å. The close-packed directions are labeled as: $[00\bar{1}]$, $[1\bar{1}0]$, and $[10\bar{1}]$. Additionally, the (111) surface for noble metals exhibits a Shockley surface state [57] with the Cu(111) band minimum located at 450 mV below Fermi energy.

After sample preparation, STM overview images are gathered in order to visually ensure that no molecules remain from prior experiments. Cu(111) was scanned at increasingly smaller tip-sample distances in order to verify that the tip is metallic. In 3.3 (a), large Cu(111) islands are present while individual copper adatoms are visible at closer tip-sample distances due to their bright contrast, as seen in Fig 3.3 (b). In Fig 3.3, additional scans reveal the Cu(111) surface with atomic scale contrast.

3.4 Tip Preparation

In order to prepare the CO tip to investigate the intermediate states, the CO coverage on the prepared Cu(111) surface should be low. After any contamination has been removed, then the sample is placed inside the microscope. Initially, the tip is brought in contact with the surface to yield a Cu-covered tip apex. CO is leaked from the gas lines into the preparation chamber until it reaches a pressure of approximately 1×10^{-6} mbar. The ion getter guns are switched off in both the prep and STM chambers with the valve between the two chambers open. The sample is allowed to cool to approximately 4.2 K before the cryoshield is opened for 15s and then closed again. The sample is allowed to cool down to approximately 4.2 K before the tip is approached to the sample.

In Fig 3.5 (a), the STM image shows the standing wave pattern of the Cu(111) surface state electrons which scatter at defects. The defects present are small and large depressions having a larger apparent depth. The latter are identified as CO molecules, due to the increase in coverage as additional CO is leaked into the chamber.

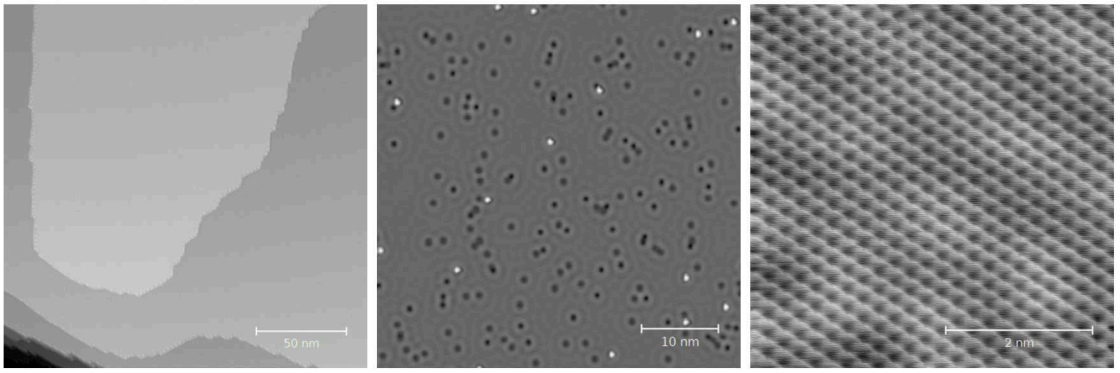

(a) (b) (c)

Figure 3.3: STM images of a cleaned Cu(111) surface after repeated annealing and sputtering cycles. (a) STM overview image of large Cu(111) terraces (I = 5.3E-10 A, V_{Bias} = 0.306V). (b) STM image of Cu(111) surface with high contrast protrusions being Cu adatoms (I = 2.1E-10 A, V_{Bias} = 0.293V). (c) STM image of Cu(111) showing atomic resolution of the surface (I = 2.5E-8 A, V_{Bias} = 0.002V)

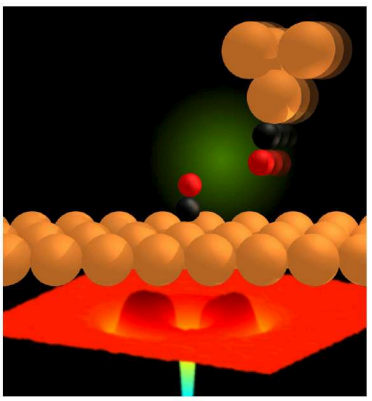

(a)

Figure 3.4: 3D simulation of a metallic STM tip with attached CO molecule at apex. Reprinted with permission from [58].

In order to pursue the experiments in the thesis, the CO molecule must be attached to the tip apex. This is done by bringing the tip over the desired CO molecule, then manipulating the CO molecule so that the carbon atom will bind to the copper tip apex with the oxygen molecule facing out towards the surface[59][60].

After scanning over the surface and identifying the CO molecule, a vertical manipulation procedure used to affix the CO molecule to the tip apex. Starting from a setpoint current I = 3.0E-10 A, the tip approach length should be set for 10s and a V_{bias} = 2.6V. Reliability with this approach has been quite high and with consistent CO pickups. To verify that a CO tip is attached, the sample area is scanned again to verify the contrast change as seen in Fig 3.5 (b).

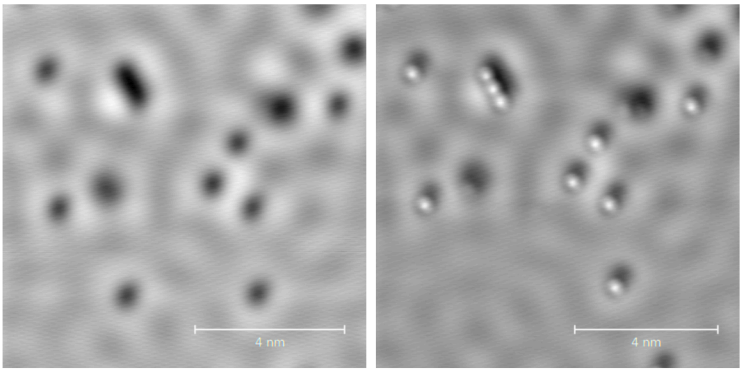

(a) (b)

Figure 3.5: STM images of a Cu(111) surface with deposited CO molecules (I = 3.1E-10 A, V_{Bias} = 0.102V). Left image (a) shows an STM image of a metallic tip, while the right image (b) shows an STM image of a CO functionalized tip after CO pickup.

3.5 Software

All of the software for controlling the STM/AFM equipment is provided by the manufacturer or is freely available to download. The primary control software, STMAFM, is built and distributed by Createc and operates the primary functions related to the STM, piezo control, and other hardware. The Nanonis SPM Controller software operates the external PLL for operating the qPlus sensor in AFM mode. Image processing is performed using the WSxM software and Gwyddion with some additional adjustments performed through custom-built scripts.

Adjustments were made to the Createc software to automate manual scanning features native to the software. This was primarily used to automate the collection of KPFM data and was performed through a Matlab interface in the Createc software. This was done due to the length of the scans and the need for the operator to be at the workstation to commence the next scan. By automating this process, it eliminated the need for an operator to be present and allowed scans to continue through non-working hours.

4 Results and Discussion

In this chapter, the evolution of a planar organic molecule (3,9(10)-DBP) with a Cu(111) surface is presented. Combining three experimental techniques of STM, AFM, and KPFM, the details of the evolution of the molecule to 5-AGNR are revealed. The molecules are influenced by the metallic surface below them, driving the self-assembly process and acting to help form an organometallic framework, leading to the formation of 5-AGNR. The results are presented in this chapter along with the discussion.

4.1 3,9(10)-DBP/Cu(111) to GNR

The investigated molecule 3,9(10)-dibromoperylene (3,9(10)-DBP, $C_{20}H_{10}Br_2$, M = 410.101 Da) is illustrated in Fig 4.1 a molecule consisting of a perylene core with two bromines attached in a parallel or anti-parallel arrangement. The planar structure of the molecule makes it ideal for analysis with surface-sensitive techniques. Experimental studies have confirmed the formation of armchair 5-AGNR on Au(111)[19] and Cu(111)[18]. While the formation of 5-AGNR on Cu(111) has been studied, more in-depth investigations are necessary to confirm the reaction process.

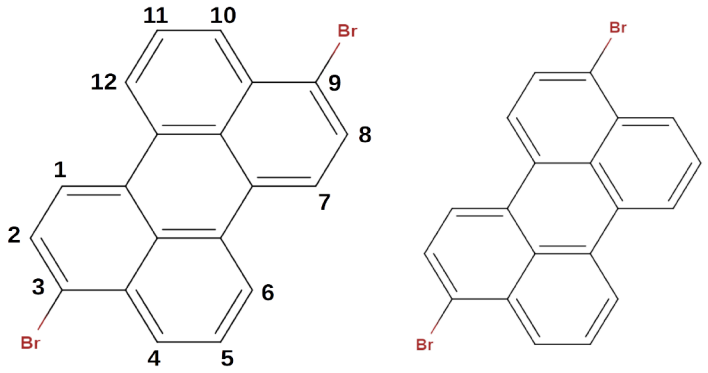

(a) (b)

Figure 4.1: (a-b) Two dimensional wireframe representations of the 3,9(10)-DBP/Cu(111) precursor molecules.

4.2 DBP on Cu(111) - 200 K

Single 3,9(10)-DBP molecules are distributed randomly over the surface when deposited on to a cold Cu(111) surface (T = 200 K) and allowed to cool again to T = 5 K, as shown in Fig 4.2 (a). Molecules were found to cluster in dimers, trimers, and along step edges, signaling that there is some diffusion at low temperatures. At T = 5K, molecules remained in place with minimal drift. Dimer and trimers were found to be oriented around the bromines at C3(C4) or C9(C10). Fig 4.2 (b) shows a high-resolution STM that single 3,10-DBP molecules are seen as a distorted trapezoid, with two lobes at the ends representing the bromines, while four lobes

between them represent the carbon rings. Also present are two partially debromiated DBP molecules with a single bromine at C9(10) still oriented towards the center of the trimer. The bromine is still present, slightly displaced from its original position. More clearly visible are the carbon rings, which are slightly pulled down towards the surface. From Fig 4.2 (c), it is clear that the lobes on the ends correspond to the bromines while the carbon rings can be assigned to the interior lobes. While the

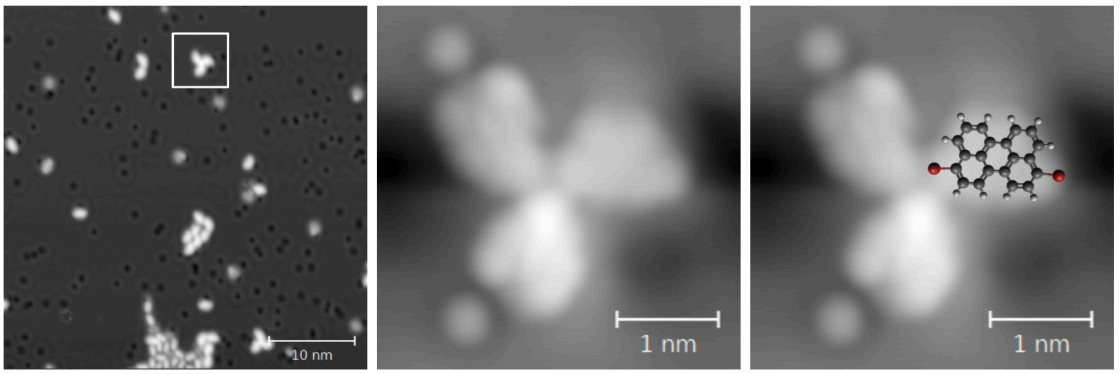

(a) (b) (c)

Figure 4.2: 3,9(10)-DBP/Cu(111) deposition at T = 200 K (I = 1.1E-10A, Bias = 0.391V). (a) Overview STM image of self-assembled DBP molecules on Cu(111) with a CO functionalized tip. Single molecules are spread over the surface, but have self-assembled into dimer and trimers (600x600 Å^2). The area marked with a square is enlarged in (b) and (c). (b) High resolution STM image shows a trimer, where three DBP molecules have oriented around the attached bromine. Two of the DBP molecules show detached bromines, located near C3 (C4). (c) The molecular structure of the 3,10-DBP molecule is overlaid on the image in (b), showing that end lobes correspond to the position of the bromines.

high-resolution STM images can provide the overall topography of the molecule, it cannot provide a confirmation of the chemical structure. In order to achieve atomic scale contrast, it is necessary to operate in the region where short-range chemical forces enhance the image contrast. To further improve the sensitivity of the to these short-range forces, small oscillation amplitudes (0.5 Å) were used[38]. Imaging the molecules in constant-height mode additionally allows for stable operation, even if the frequency shift Δf(z) is nonmonotonically related to distance.

In Fig 4.3 (a), a constant-height AFM image of a trimer structure of 3,9(10)DBP is shown, recorded at a $V_{Bias} = 0.105$V. At this voltage value, the molecule appears as a flat structure, with a four ring structure connected to two bright lobes. The 3,10-DBP structure is clearly visible, with two bromines attached in a parallel configuration at C3(4) and C9(10). The two other molecules present show clearly only two ring structures and a bright lobe, where all three molecules are oriented around the bright lobes. This configuration suggests that the molecules have become debromiated and that the two other ring structures are pulling down towards the surface. Between two of the DBP molecules is an area of bright contrast. From earlier STM images and finding CO randomly deposited across the surface, this is a CO molecule that

has adsorbed on the surface between the two molecules.

Also seen is high contrast between the bromines, suggesting that the three molecules have become bonded by the bromines. No chemical bonds have occurred and instead this overly high resolution can be described as the CO bending, resembling the chemical bonds of the molecules[53]. In order to justify the chemical structure found by the AFM images, atomic resolution KPFM was explored to measure the charge distribution of the molecule. Fig 4.3 (b) shows an LCPD image of the trimer structure, which does resemble that of the AFM image while Fig 4.3 (c) shows the simultaneously measured Δf, confirming the AFM image in (a).

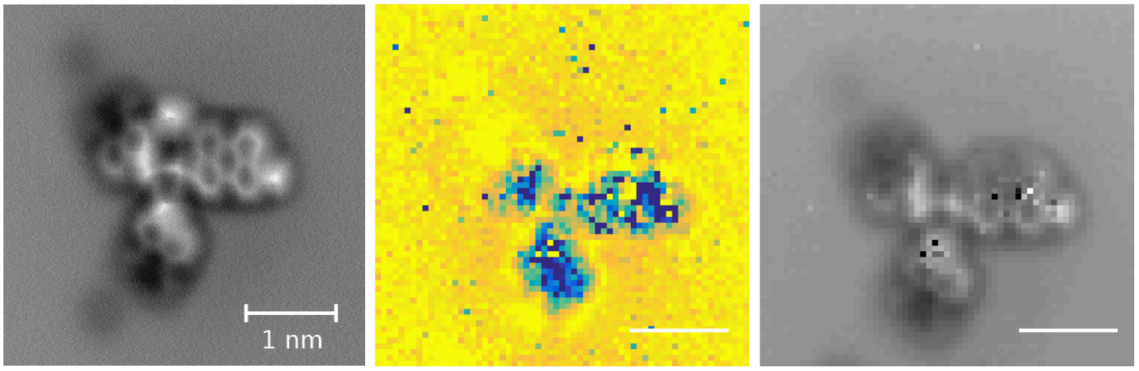

(a) (b) (c)

Figure 4.3: (a) Constant-height AFM and KPFM imaging of 3,9(10)-DBP on Cu(111). (a) AFM constant-height image of DBP trimer recorded with a CO-terminated tip recorded from the STM set point (I = 1.0E-10A, V_{Bias} = 0.1V). (b) LCPD image recorded with same tip and imaging parameters as (a). Color ranges from 400mV (yellow) to -400 mV (blue). (c) Δf image measured simultaneously with the LCPD signal. Color ranges from 0 (white) to -15 Hz (black). The line in (b) and (c) correspond to 1 nm.

4.3 DBP on Cu(111) - 300 K

In order to understand the evolution of the DBP and determine the coupling mechanism, the sample was taken through a series of annealing cycles. The sample was annealed starting at T = 300 K for 15 minutes, before being cooled back to T = 5 K. In Fig 4.4 (a), molecules were found to form long chains oriented along the bromines. While appearing to be bonded, they show a the same molecular structure as those reported at 200 K, shown in 4.4 (b). 4.4 (c) shows the DBP molecule overlaid on the STM image. Again, the chains form with both the 3,9- and 3,10-DBP molecules, the only difference is that the C3(4) and C9(10) bromines now predominantly orient in a parallel configuration.

In Fig 4.5 (a), the chemical structure becomes apparent when imaged with CO-terminated tip. The increase in contrast at the bottom of the the molecules results from an incorrect planar correction. The LCPD map in Fig 4.5 (b) shows a similar structure to the constant-height AFM image, showing sub-molecular resolution for

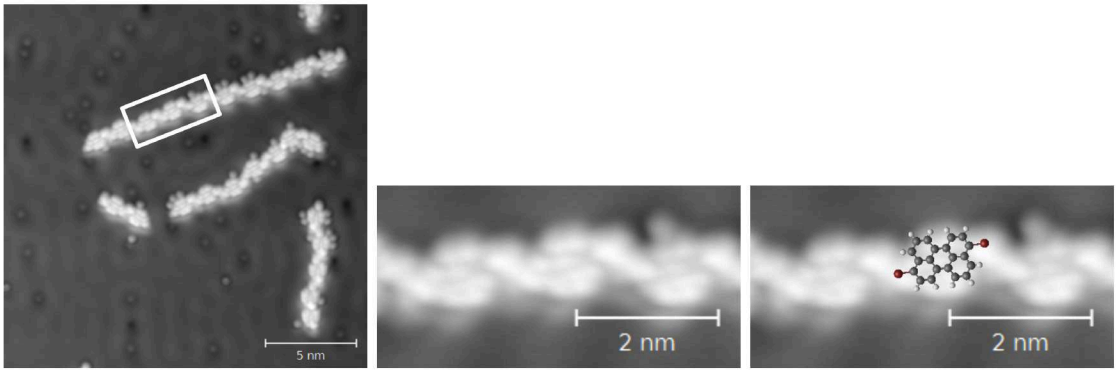

(a) (b) (c)

Figure 4.4: 3,9(10)-DBP/Cu(111) annealing to T = 300 K. (a) Overview STM image of self-assembled DBP molecules on Cu(111) with a CO functionalized tip (I = 1.1E-10A, V_{Bias} = 0.1V). Single molecules are spread over the surface, but have self-assembled into long chains, arranged along the bromines (50x50 Å^2). The area marked with a square is enlarged in (b) and (c). (b) High resolution STM image shows a part of this chain, where three DBP molecules have oriented along the attached bromines (I = 3E-10A, V_{Bias} = 0.1V). (c) The molecular structure of the 3,9- and 3,10-DBP molecules are overlaid on the image in (b), showing that the individual molecules are unchanged.

these planar structures. The utilization of this method helps provide a qualitative description that the molecular structure seen in the AFM images. Fig 4.5 (c) shows a Δf image measured simultaneously with the LCPD map and is seen to match that of the separate AFM image.

4.4 DBP on Cu(111) - 480 K

The results of further evaporation of additional DBP molecules and annealing of the sample to T = 480 K are shown in Fig 4.6 (a). Long chains of molecules have formed, with strong contrast periodically along the chain. Surrounding the chains are circular protrusions which correspond to bromines that have been cleaved from C3(4) and C9(10). In Fig 4.6 (b), a high resolution STM image shows more clearly the surrounding bromines and higher contrast regions inside the chain, while (c) shows the predicted molecular structure consisting of a perylene unit interconnected with Cu atoms from the surface.

With AFM and KPFM, it is shown in Fig 4.7 (a) that the chemical structure consists of the perylene core and that the bromines have been cleaved from the molecule, now surrounding the chains. From the figure, it appears as though the perylene cores are now forming covalent bonds, but bond length measurement between C3(4) and C9(10) positions of adjacent perylene cores show 3.5 ± 0.5 Å, too long for a covalent carbon-carbon bond. From the bond length and contrast seen in the STM images, the explanation for this bond is the introduction of copper atoms into the chain[61], forming organometallic chains, which increases the stability of the perylene

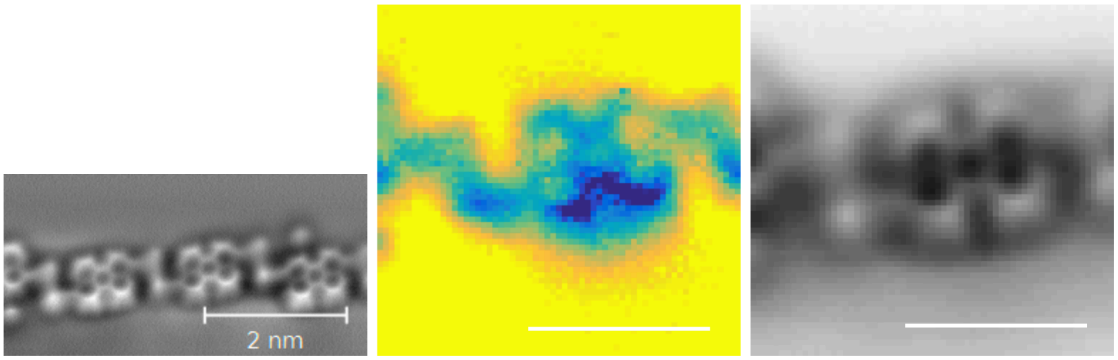

(a) (b) (c)

Figure 4.5: Constant-height AFM and KPFM imaging of 3,9(10)-DBP on Cu(111). (a) AFM constant-height image of DBP chain recorded with a CO-terminated tip recorded from the STM set point (I = 3E-10A, V_{Bias} = 0.1V). (b) LCPD image recorded with same tip and imaging parameters as (a). Color ranges from 280mV (yellow) to 100 mV (blue). (c) Δf image measured simultaneously with the LCPD signal. Color ranges from 5 (white) to -15 Hz (black). The line in (b) and (c) correspond to 1 nm.

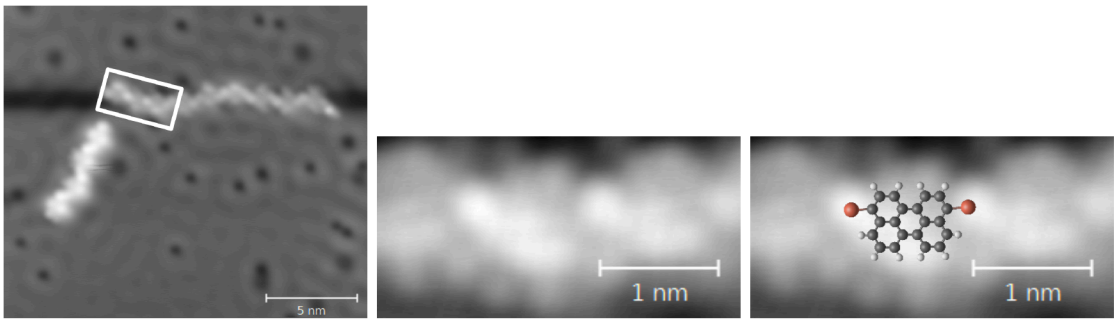

(a) (b) (c)

Figure 4.6: 3,9(10)-DBP/Cu(111) annealing to T = 480 K. (a) Overview STM image of self-assembled DBP molecules on Cu(111) with a CO functionalized tip (I = 1.0E-10A, V_{Bias} = 0.1V). Additional evaporation of DBP molecules and annealing show a self-assembly into long chains surrounded by protrusions and chain units interconnect with bright contrast (200x200 Å^2). The area marked with a square is enlarged in (b) and (c). (b) High resolution STM image shows a part of this chain, where perylene bi-radicals are stabilized with copper atoms. (c) The molecular structure of the perylene units and copper atoms are overlaid on the image in (b). Lines on (b) and (c) represent 1 nm.

cores after the cleaving of the bromines. In Fig 4.7 (b), the LCPD map shows a similar structure to that of the AFM image in (a), while (c) shows a separately measured Δf image. The LCPD map provides qualitative evidence position of the bond locations and that copper atoms are stabilizing the perylene biradical. When combined with Fig 4.7 (c), it can confirm the AFM image seen in (a).

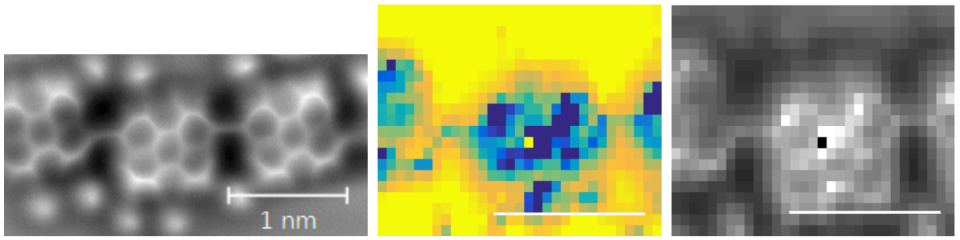

(a) (b) (c)

Figure 4.7: Constant-height AFM and KPFM imaging of perylene bi-radical on Cu(111). (a) AFM constant-height image of perylene bi-radical chain recorded with a CO-terminated tip recorded from the STM set point (I = 2.5E-10A, V_{Bias} = 0.1V). (b) LCPD image recorded with same tip and imaging parameters as (a). Color ranges from 0 (yellow) to -1500 mV (blue). (c) Δf image measured simultaneously with the LCPD signal. Color ranges from 5 (white) to -15 Hz (black). The line in (b) and (c) correspond to 1 nm.

4.5 DBP on Cu(111) - 530 K

The result of additional DBP evaporation and annealing to T = 530 K is shown in Fig 4.8 (a), where straight chains have formed. The length of the chains has been reduced compared to previous annealing temperatures. Where the previous annealing temperature showed a single apparent bond between adjacent perylene units, the remaining C3(4) or C9(10) shows an apparent bond as well, as seen in Fig 4.8 (b). The bright contrast seen here as well as at T = 480 K suggests that another copper atom has been introduced into the chain, as shown in Fig 4.8 (c), forming a perylene-tetradical.

Confirmation of the molecular structure can be seen in Fig 4.9 (a), where each perylene unit is interconnected at the C3(4) and C9(10) locations. Similar to the bi-radical formation, the bond lengths are still too long for a covalent carbon-carbon bond. Additionally, the contrast change between the units suggests that the carbon rings are being pulled down towards the surface. Since the STM shows an extremely bright feature located between the units and each unit shows equivalent contrast, it can be concluded that perylene tetradicals have formed, which are stabilized by the organometallic chains connected by copper atoms. This can be confirmed in Fig 4.9 (b) which shows a similar structure to the constant-height AFM images and clearly showing the charge between the structures. The Δf image in Fig 4.9 (c), taken at the same time as the LCPD map, supports the structure of the constant-height AFM image in (a).

4.6 DBP on Cu(111) - 560 K

In order to confirm that Ullmann coupling is the reaction mechanism that takes places in the evolution of DBP to GNR, additional DBP molecules were evaporated onto the surface and annealed to T = 560 K. As seen in Fig 4.10, short ribbons of 5-AGNR (a) or large clusters of molecules (b-c) were common, whereas longer ribbon

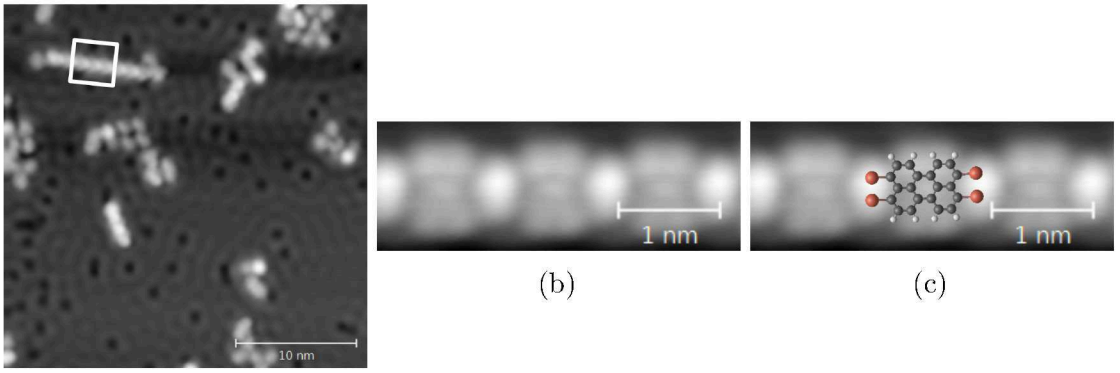

(a) (b) (c)

Figure 4.8: 3,9(10)-DBP/Cu(111) annealing to T = 530 K. (a) Overview STM image of self-assembled DBP molecules on Cu(111) with a CO functionalized tip (I = 1.0E-10A, V_{Bias} = 0.1V). Additional evaporation of DBP molecules and annealing show a self-assembly into long, straight chains with chains units interconnect with areas of bright contrast (300x300 Å^2). The area marked with a square is enlarged in (b) and (c). (b) High resolution STM image shows a part of this chain, where three perylene units have attached at C3(4) and C9(10). (I = 1.0E-10A, V_{Bias} = 0.1V) (c) The molecular structure of the perylene units and copper atoms are overlaid on the image in (b).

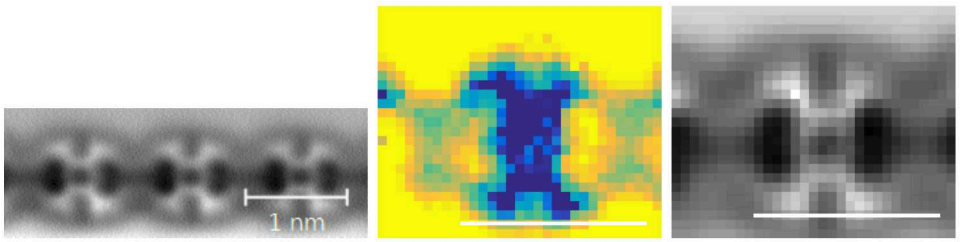

(a) (b) (c)

Figure 4.9: Constant-height AFM and KPFM imaging of perylene tetradical on Cu(111). (a) AFM constant-height image of perylene tetradical recorded with a CO-terminated tip recorded from the STM set point (I = 1.0E-10A, V_{Bias} = 0.1V). (b) LCPD image recorded with same tip and imaging parameters as (a). Color ranges from 0mV (yellow) to -500 mV (blue). (c) Δf image measured simultaneously with the LCPD signal. Color ranges from -2 (white) to -8 Hz (black). The line in (b) and (c) correspond to 1 nm.

structures as seen on Au(111)[19] were not seen. This reduced ribbon quality comes as a result of the Cu(111) surface itself, where an increase in radical sites reduces the diffusion of the molecules[62].

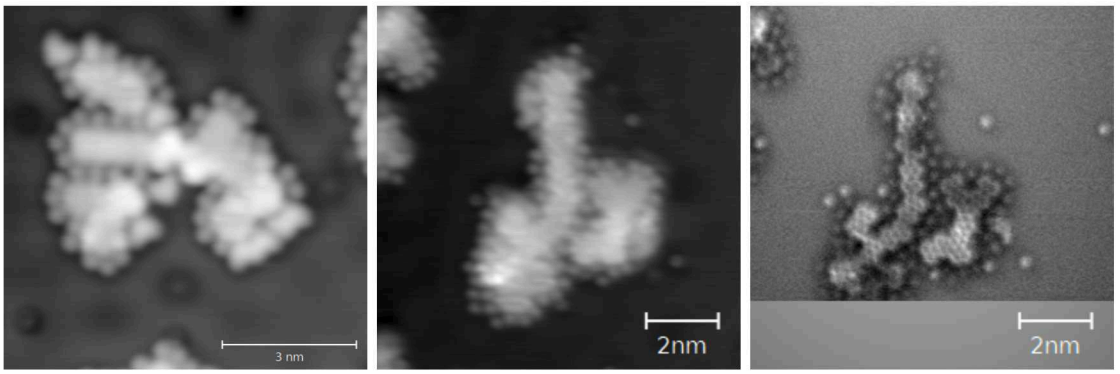

(a) (b) (c)

Figure 4.10: 3,9(10)-DBP/Cu(111) annealing to T = 560 K. STM images of self-assembled DBP molecules on Cu(111) with a CO functionalized tip (I = 1.0E-10A, V_{Bias} = 0.1V). (a) Additional evaporation of DBP molecules and annealing show a self-assembly into small graphene nanoribbons (300x300 Å^2). (b-c) STM image showing a self-assembly of perylene cores, but without any confirmed nanoribbon formation.

5 Conclusion and Future Work

In this thesis, the objectives of this thesis were to determine the reaction mechanism for the growth of graphene nanoribbons from 3,9(10) dibromoperylene utilizing scanning tunneling, atomic force, and kelvin probe force microscopies. This addition of the KPFM complemented the high-resolution imaging by STM and AFM by providing qualitative data to sub-molecular resolution.

By starting with evaporation of DBP molecules onto a clean Cu(111) surface at low temperatures, it was possible to confirm how DBP molecules organize, providing an understanding for results at higher annealing temperatures. The AFM and LCPD maps supported conclusions about the molecular structure and how debromiated molecules behave, as the radical site becomes stabilized by the copper surface. In the second experiment, higher temperatures caused the DBP molecules to rearrange into long, uneven chains, without changing the DBP molecule itself. AFM and LCPD maps confirmed that the structure of the molecules, in addition to their chain orientation.

In the third experiment, increased annealing temperatures provided evidence of the reaction mechanism and the influence of the copper surface. From STM, it was possible to observe a strong contrast change at the binding site, signaling the introduction of an intermediary atom which stabilized the perylene bi-radical structure. This was confirmed with AFM and the LCPD maps which showed that bond lengths were too long for a covalent carbon-carbon bond.

Finally, the sample was annealed further, which confirmed the reaction mechanism as Ullmann coupling, demonstrating the critical role the surface plays in the formation of these nanoribbons. The STM data showed a significantly brighter contrast than in the prior bi-radical structure, providing the possibility that an additional copper atom has been introduced into the chain. This was confirmed with AFM and LCPD maps made of the chain, showing the bond lengths and charge location, providing qualitative evidence towards the conclusion that a perylene tetradical structure was formed.

While individually STM, AFM, and KPFM are powerful tools for the investigation of single molecule properties, when combined, they offer a comprehensive way of confirming analysis on changes in a system, discovering reaction pathways, and a more detailed investigation into various systems. In order to ensure that this growth mechanism is correct, further work needs to be done on investigating the copper atom in the bonds. Questions remain about if it is raised out of the surface or derives from adatoms found on the surface. Further work with these three combined techniques and the knowledge acquired thus far will allow for confirmation of this coupling mechanism.

References

[1] G. Moore, "Progress In Digital Integrated Electronics [Technical literaiture, Copyright 1975 IEEE. Reprinted, with permission. Technical Digest. International Electron Devices Meeting, IEEE, 1975, pp. 11-13.]," *IEEE Solid-State Circuits Newsletter*, vol. 20, no. 3, pp. 36–37, 2006. [Online]. Available: http://ieeexplore.ieee.org/lpdocs/epic03/wrapper.htm?arnumber=4804410

[2] R. Courtland, "Intel Finds Moore's Law's Next Step at 10 Nanometers," 2016. [Online]. Available: http://spectrum.ieee.org/semiconductors/devices/intel-finds-moores-laws-next-step-at-10-nanometers

[3] F. Schwierz, "Graphene transistors." *Nat. Nanotechnol.*, vol. 5, no. July, p. 487, 2010. [Online]. Available: http://www.ncbi.nlm.nih.gov/pubmed/20512128

[4] A. Aviram and M. A. Ratner, "Molecular rectifiers," *Chemical Physics Letters*, vol. 29, no. 2, pp. 277–283, 1974.

[5] G. J. Ashwell, J. R. Sambles, A. S. Martin, W. G. Parker, and M. Szablewski, "Rectifying characteristics of Mg|(C16H33-Q3CNQ LB film)|Pt structures," *Journal of the Chemical Society, Chemical Communications*, pp. 1374–1376, 1990. [Online]. Available: http://dx.doi.org/10.1039/C39900001374

[6] A. S. Martin, J. R. Sambles, and G. J. Ashwell, "Molecular rectifier," *Physical Review Letters*, vol. 70, no. 2, pp. 218–221, 1993.

[7] R. M. Metzger, B. Chen, U. Höpfner, M. V. Lakshmikantham, D. Vuillaume, T. Kawai, X. Wu, H. Tachibana, T. V. Hughes, H. Sakurai, J. W. Baldwin, C. Hosch, M. P. Cava, L. Brehmer, and G. J. Ashwell, "Unimolecular electrical rectification in hexadecylquinolinium tricyanoquinodimethanide," *Journal of the American Chemical Society*, vol. 119, no. 43, pp. 10 455–10 466, 1997.

[8] K. S. Novoselov, A. K. Geim, S. V. Morozov, D. Jiang, Y. Zhang, S. V. Dubonos, I. V. Grigorieva, and A. A. Firsov, "Electric field effect in atomically thin carbon films." *Science (New York, N.Y.)*, vol. 306, no. 5696, pp. 666–669, 2004. [Online]. Available: http://www.ncbi.nlm.nih.gov/pubmed/15499015

[9] M. Y. Han, B. Özyilmaz, Y. Zhang, and P. Kim, "Energy band-gap engineering of graphene nanoribbons," *Physical Review Letters*, vol. 98, no. 20, 2007.

[10] K. Nakada, M. Fujita, G. Dresselhaus, and M. S. Dresselhaus, "Edge state in graphene ribbons: Nanometer size effect and edge shape dependence," *Physical Review B*, vol. 54, no. 24, pp. 17 954–17 961, 1996.

[11] P. Ruffieux, S. Wang, B. Yang, C. Sánchez-Sánchez, J. Liu, T. Dienel, L. Talirz, P. Shinde, C. A. Pignedoli, D. Passerone, T. Dumslaff, X. Feng, K. Müllen, and R. Fasel, "On-surface synthesis of graphene nanoribbons with zigzag edge topology," *Nature*, vol. 531, no. 7595, pp. 489–492, 2016. [Online]. Available: http://www.nature.com/doifinder/10.1038/nature17151

[12] X. R. Wang and H. J. Dai, "Etching and narrowing of graphene from the edges," *Nat Chem*, vol. 2, no. 8, pp. 661–665, 2010.

[13] J. V. Barth, G. Costantini, and K. Kern, "Engineering atomic and molecular nanostructures at surfaces," *Nature*, vol. 437, no. 7059, pp. 671–679, 2005. [Online]. Available: http://www.nature.com/doifinder/10.1038/nature04166

[14] J. Cai, P. Ruffieux, R. Jaafar, M. Bieri, T. Braun, S. Blankenburg, M. Muoth, A. P. Seitsonen, M. Saleh, X. Feng, K. Müllen, and R. Fasel, "Atomically precise bottom-up fabrication of graphene nanoribbons." *Nature*, vol. 466, no. 7305, pp. 470–3, 2010. [Online]. Available: http://www.nature.com/nature/journal/v466/n7305/full/nature09211.html?free=2

[15] J. Cai, C. A. Pignedoli, L. Talirz, P. Ruffieux, H. Söde, L. Liang, V. Meunier, R. Berger, R. Li, X. Feng, K. Müllen, and R. Fasel, "Graphene nanoribbon heterojunctions," *Nature Nanotechnology*, vol. 9, no. 11, pp. 896–900, 2014. [Online]. Available: http://www.nature.com/doifinder/10.1038/nnano.2014.184

[16] J. Cai, P. Ruffieux, R. Jaafar, M. Bieri, T. Braun, S. Blankenburg, M. Muoth, A. P. Seitsonen, M. Saleh, X. Feng, K. Müllen, and R. Fasel, "Atomically precise bottom-up fabrication of graphene nanoribbons," *Nature*, vol. 466, no. 7305, pp. 470–473, 2010. [Online]. Available: http://www.nature.com/doifinder/10.1038/nature09211

[17] H. Huang, D. Wei, J. Sun, S. L. Wong, Y. P. Feng, A. H. C. Neto, and A. T. S. Wee, "Spatially Resolved Electronic Structures of Atomically Precise Armchair Graphene Nanoribbons," *Scientific Reports*, vol. 2, 2012. [Online]. Available: http://www.nature.com/articles/srep00983

[18] F. Schulz, P. H. Jacobse, F. F. Canova, J. van der Lit, D. Z. Gao, A. van den Hoogenband, P. Han, R. J. Klein Gebbink, M.-E. Moret, P. M. Joensuu, I. Swart, and P. Liljeroth, "Precursor Geometry Determines the Growth Mechanism in Graphene Nanoribbons," *The Journal of Physical Chemistry C*, p. acs.jpcc.6b12428, 2017. [Online]. Available: http://pubs.acs.org/doi/abs/10.1021/acs.jpcc.6b12428

[19] A. Kimouche, M. M. Ervasti, R. Drost, S. Halonen, A. Harju, P. M. Joensuu, J. Sainio, and P. Liljeroth, "Ultra-narrow metallic armchair graphene nanoribbons," *Nature Communications*, vol. 6, p. 10177, 2015. [Online]. Available: http://www.nature.com/doifinder/10.1038/ncomms10177

[20] H. Lüth, *Solid Surfaces, Interfaces and Thin Films*, 2010. [Online]. Available: http://link.springer.com/10.1007/978-3-642-13592-7

[21] D. M. Eigler and E. K. Schweizer, "Positioning single atoms with a scanning tunnelling microscope," *Nature*, vol. 344, no. 6266, pp. 524–526, 1990. [Online]. Available: http://www.nature.com/doifinder/10.1038/344524a0

[22] G. Binnig, H. Rohrer, C. Gerber, and E. Weibel, "7 x 7 Reconstruction on Si(111) Resolved in Real Space," *Physical Review Letters*, vol. 50, no. 2, pp. 120–123, 1983.

[23] G. Binnig and H. Rohrer, "Scanning tunneling microscopy," *Surface Science*, vol. 126, no. 126, pp. 236–244, 1982. [Online]. Available: http://people.ee.duke.edu/~dwyer/courses/ece310/Binnig_STM.pdf

[24] R. S. Becker, J. A. Golovchenko, D. R. Hamann, and B. S. Swartzentruber, "Real-Space Observation of Surface States on Si(111) 7??7 with the Tunneling Microscope," *Physical Review Letters*, vol. 55, no. 19, pp. 2032–2034, 1985.

[25] L. Gross, N. Moll, F. Mohn, A. Curioni, G. Meyer, F. Hanke, and M. Persson, "High-Resolution Molecular Orbital Imaging Using a p-Wave STM Tip," *Physical Review Letters*, vol. 107, no. 8, p. 086101, 2011. [Online]. Available: http://link.aps.org/doi/10.1103/PhysRevLett.107.086101

[26] B. E. Murphy, "The physico-chemical properties of fullerenes and porphyrin derivatives deposited on conducting surfaces," no. February, p. 227, 2014. [Online]. Available: http://hdl.handle.net/2262/77400

[27] C. J. Chen, "Introduction to Scanning Tunneling Microscopy Second Edition," *Oxford University Press*, p. (2008), 2008.

[28] J. Bardeen, "Tunnelling from a many-particle point of view," *Phys. Rev. Lett.*, vol. 6, no. 2, p. 57, 1961.

[29] A. D. Gottlieb and L. Wesoloski, "Bardeen's tunnelling theory as applied to scanning tunnelling microscopy: a technical guide to the traditional interpretation," *Nanotechnology*, vol. 17, no. 8, pp. R57–R65, 2006. [Online]. Available: http://stacks.iop.org/0957-4484/17/i=8/a=R01?key=crossref.bc22daa1f15b42589baa336aa2aefaf8

[30] J. Tersoff and D. Hamann, "Theory and application for the scanning tunneling microscope," *Physical review letters*, vol. 50, no. 25, p. 1998, 1983. [Online]. Available: http://journals.aps.org/prl/abstract/10.1103/PhysRevLett.50.1998

[31] D. J. Griffiths, *Introduction to Quantum Mechanics*, 2005, vol. 1. [Online]. Available: http://books.google.com/books?id=ipCxQgAACAAJ

[32] G. Binnig, C. F. Quate, and C. Gerber, "Atomic force microscope," *Physical Review Letters*, vol. 56, no. 9, pp. 930–933, 1986.

[33] G. Binnig, C. Gerber, E. Stoll, T. R. Albrecht, and C. F. Quate, "Atomic Resolution with Atomic Force Microscope," *Europhysics Letters (EPL)*, vol. 3, no. 12, pp. 1281–1286, 1987. [Online]. Available: http://stacks.iop.org/0295-5075/3/i=12/a=006?key=crossref.b4226899d693c222fce9a99f5c18b144

[34] L. Gross, Z. L. Wang, D. Ugarte, F. Mohn, N. Moll, W. a. Heer, P. Vincent, P. Liljeroth, C. Journet, G. Meyer, V. T. Binh, M. Poot, H. S. J. V. D. Zant, A. Aguasca, A. Bachtold, K. Kim, A. Zettl, P. Hung, H. W. C. Postma, M. Bockrath, X. Blase, and S. Roche, "The Chemical Structure of a Molecule Resolved by Atomic Force Microscopy," *Science*, vol. 325, no. August, pp. 1110–4, 2009. [Online]. Available: http://www.ncbi.nlm.nih.gov/pubmed/19713523

[35] F. Giessibl, "Atomic resolution on Si(111)-(7x7) by noncontact atomic force microscopy with a force sensor based on a quartz tuning fork," *Applied Physics Letters*, vol. 76, p. 1470, 2000. [Online]. Available: http://scitation.aip.org/content/aip/journal/apl/76/11/10.1063/1.126067

[36] F. Mohn, L. Gross, N. Moll, and G. Meyer, "Imaging the charge distribution within a single molecule," *Nature Nanotechnology*, vol. 7, no. 4, pp. 227–231, 2012. [Online]. Available: http://dx.doi.org/10.1038/nnano.2012.20

[37] D. S. Wastl, A. J. Weymouth, and F. J. Giessibl, "Optimizing atomic resolution of force microscopy in ambient conditions," *Physical Review B - Condensed Matter and Materials Physics*, vol. 87, no. 24, 2013.

[38] F. J. Giessibl, "Advances in atomic force microscopy," *Reviews of Modern Physics*, vol. 75, no. 3, pp. 949–983, 2003.

[39] ——, *Noncontact Atomic Force Microscopy*, vol. 3.

[40] F. Giessibl, "Forces and frequency shifts in atomic-resolution dynamic-force microscopy," *Physical Review B*, vol. 56, no. 24, pp. 16 010–16 015, 1997.

[41] J. E. Sader and S. P. Jarvis, "Accurate formulas for interaction force and energy in frequency modulation force spectroscopy," *Applied Physics Letters*, vol. 84, no. 10, pp. 1801–1803, 2004. [Online]. Available: http://aip.scitation.org/doi/10.1063/1.1667267

[42] A. Paulo and R. Garcia, "Unifying theory of tapping-mode atomic-force microscopy," *Physical Review B*, vol. 66, no. 4, pp. 2–5, 2002.

[43] R. García, *Dynamic atomic force microscopy methods*, 2002, vol. 47, no. 6-8. [Online]. Available: http://www.sciencedirect.com/science/article/pii/S0167572902000778

[44] N. Kocić, S. Decurtins, S. X. Liu, and J. Repp, "Forces from periodic charging of adsorbed molecules," *Journal of Chemical Physics*, vol. 146, no. 9, 2017.

[45] J. E. Jones, "On the Determination of Molecular Fields. I. From the Variation of the Viscosity of a Gas with Temperature," *Proceedings of the Royal Society A: Mathematical, Physical and Engineering Sciences*, vol. 106, no. 738, pp. 441–462, 1924. [Online]. Available: http://rspa.royalsocietypublishing.org/content/106/738/441

[46] P. M. Morse, "Diatomic molecules according to the wave mechanics. II. Vibrational levels," *Physical Review*, vol. 34, no. 1, pp. 57–64, 1929.

[47] P. Günther, U. C. Fischer, and K. Dransfeld, "Scanning near-field acoustic microscopy," *Applied Physics B Photophysics and Laser Chemistry*, vol. 48, no. 1, pp. 89–92, 1989.

[48] H. Edwards, L. Taylor, W. Duncan, and A. J. Melmed, "Fast, high-resolution atomic force microscopy using a quartz tuning fork as actuator and sensor," *Journal of Applied Physics*, vol. 82, no. 3, pp. 980–984, 1997. [Online]. Available: http://jap.aip.org/resource/1/japiau/v82/i3/p980_s1%5Cnhttp://scitation.aip.org/getpdf/servlet/GetPDFServlet?filetype=pdf&id=JAPIAU000082000003000980000001&idtype=cvips&doi=10.1063/1.365936&prog=normal

[49] F. J. Giessibl, "High-speed force sensor for force microscopy and profilometry utilizing a quartz tuning fork," *Applied Physics Letters*, vol. 73, no. 26, pp. 3956–3958, 1998.

[50] B. Babic, C. Freund, J. Herrmann, and J. Miles, "Metrological scanning probe microscope based on a quartz tuning fork detector," *J. Micro/Nanolith. MEMS MOEMS*, vol. 11, no. 1, pp. 011 003–1, 2012. [Online]. Available: http://nanolithography.spiedigitallibrary.org/article.aspx?articleid=1183473

[51] N. Moll, L. Gross, F. Mohn, A. Curioni, and G. Meyer, "The mechanisms underlying the enhanced resolution of atomic force microscopy with functionalized tips," *New Journal of Physics*, vol. 12, no. 111, 2010.

[52] G. Blyholder, "Molecular orbital view of chemisorbed carbon monoxide," *Journal of Physical Chemistry A*, vol. 68, no. 1, p. 2772–2777, 1964. [Online]. Available: http://pubs.acs.org/doi/abs/10.1021/j100792a006

[53] S. K. Hämäläinen, N. Van Der Heijden, J. Van Der Lit, S. Den Hartog, P. Liljeroth, and I. Swart, "Intermolecular contrast in atomic force microscopy images without intermolecular bonds," *Physical Review Letters*, vol. 113, no. 18, 2014.

[54] J. Tersoff and D. R. Hamann, "Theory of the scanning tunneling microscope," *Physical Review B*, vol. 31, no. 2, pp. 805–813, 1985.

[55] M. Nonnenmacher, M. P. O'Boyle, and H. K. Wickramasinghe, "Kelvin probe force microscopy," *Applied Physics Letters*, vol. 58, no. 25, pp. 2921–2923, 1991.

[56] W. Melitz, J. Shen, A. C. Kummel, and S. Lee, "Kelvin probe force microscopy and its application," *Surface Science Reports*, vol. 66, no. 1, pp. 1–27, 2011. [Online]. Available: http://dx.doi.org/10.1016/j.surfrep.2010.10.001

[57] W. Shockley, "On the surface states associated with a periodic potential," *Physical Review*, vol. 56, no. 4, pp. 317–323, 1939.

[58] A. J. Weymouth, T. Hofmann, and F. J. Giessibl, "Quantifying Molecular Stiffness and Interaction with Lateral Force Microscopy," *Science*, vol. 343, no. 6175, pp. 1120–1122, 2014. [Online]. Available: http://www.sciencemag.org/cgi/doi/10.1126/science.1249502

[59] L. Bartels, G. Meyer, K.-H. Rieder, D. Velic, E. Knoesel, a. Hotzel, M. Wolf, and G. Ertl, "Dynamics of Electron-Induced Manipulation of Individual CO Molecules on Cu(111)," *Physical Review Letters*, vol. 80, no. 9, pp. 2004–2007, 1998.

[60] H. J. Lee, "Single-Bond Formation and Characterization with a Scanning Tunneling Microscope," *Science*, vol. 286, no. 5445, pp. 1719–1722, 1999.

[61] J. Park, K. Y. Kim, K. H. Chung, J. K. Yoon, H. Kim, S. Han, and S. J. Kahng, "Interchain interactions mediated by Br adsorbates in arrays of metal-organic hybrid chains on Ag(111)," *Journal of Physical Chemistry C*, vol. 115, no. 30, pp. 14 834–14 838, 2011.

[62] M. Bieri, M. T. Nguyen, O. Gr??ning, J. Cai, M. Treier, K. A??t-Mansour, P. Ruffieux, C. A. Pignedoli, D. Passerone, M. Kastler, K. M??llen, and R. Fasel, "Two-dimensional polymer formation on surfaces: Insight into the roles of precursor mobility and reactivity," *Journal of the American Chemical Society*, vol. 132, no. 46, pp. 16 669–16 676, 2010.